




Review

Halide Perovskite Single Crystals: Optoelectronic Applications and Strategical Approaches

Yurou Zhang ¹, Miaoqiang Lyu ¹, Tengfei Qiu ¹, Ekyu Han ¹, Il Ku Kim ², Min-Cherl Jung ³ , Yun Hau Ng ⁴ , Jung-Ho Yun ^{1,*}  and Lianzhou Wang ^{1,*}

- ¹ Nanomaterials Centre, School of Chemical Engineering, Australian Institute for Bioengineering and Nanotechnology (AIBN), The University of Queensland, St. Lucia, QLD 4027, Australia; yurou.zhang@uq.net.au (Y.Z.); m.lyu@uq.edu.au (M.L.); t.qiu@uq.edu.au (T.Q.); ekyu.han@uq.edu.au (E.H.)
- ² Institute of Integrated and Intelligent Systems, Griffith University, G06. 3-46, Gold Coast Campus, Parklands Drive, Southport, QLD 4125, Australia; i.kim@griffith.edu.au
- ³ Department of Materials Science, Faculty of Pure and Applied Sciences, University of Tsukuba, Ibaraki 305-8577, Japan; jung.mincherl.fp@u.tsukuba.ac.jp
- ⁴ School of Energy and Environment, City University of Hong Kong, Tat Chee Avenue, Kowloon, Hong Kong, China; yunhaung@cityu.edu.hk
- * Correspondence: j.yun1@uq.edu.au (J.-H.Y.); l.wang@uq.edu.au (L.W.); Tel.: +61-7-33361230 (J.-H.Y.)

Received: 21 July 2020; Accepted: 14 August 2020; Published: 17 August 2020



Abstract: Halide perovskite is one of the most promising semiconducting materials in a variety of fields such as solar cells, photodetectors, and light-emitting diodes. Lead halide perovskite single crystals featuring long diffusion length, high carrier mobility, large light absorption coefficient and low defect density, have been attracting increasing attention. Fundamental study of the intrinsic nature keeps revealing the superior optoelectrical properties of perovskite single crystals over their polycrystalline thin film counterparts, but to date, the device performance lags behind. The best power conversion efficiency (PCE) of single crystal-based solar cells is 21.9%, falling behind that of polycrystalline thin film solar cells (25.2%). The oversized thickness, defective surfaces, and difficulties in depositing functional layers, hinder the application of halide perovskite single crystals in optoelectronic devices. Efforts have been made to synthesize large-area single crystalline thin films directly on conductive substrates and apply defect engineering approaches to improve the surface properties. This review starts from a comprehensive introduction of the optoelectrical properties of perovskite single crystals. Then, the synthesis methods for high-quality bulk crystals and single-crystalline thin films are introduced and compared, followed by a systematic review of their optoelectronic applications including solar cells, photodetectors, and X-ray detectors. The challenges and strategical approaches for high-performance applications are summarized at the end with a brief outlook on future work.

Keywords: halide perovskite; single crystals; photovoltaics; photodetectors; optoelectronics

1. Introduction

In recent years, there has been blooming development in hybrid organic–inorganic halide perovskite materials as they possess outstanding photoelectronic properties and cost-effective low-temperature solution processability. The synthesis of a hybrid organic–inorganic halide perovskite was first reported several decades ago [1,2]. The significant attention was triggered by the development of hybrid organic–inorganic halide perovskite-sensitized photoelectrochemical cells with a power conversion efficiency (PCE) of 3.8% by Miyasaka and coworkers [3]. The study on perovskite and its derivatives has become a forefront research topic in the field of photovoltaic applications. It has been

proven that the hybrid organic–inorganic halide perovskite has tunable bandgap, long carrier diffusion length and lifetime, high carrier mobility, large light absorption coefficient, and low trap density [4–9], so are appropriate as light-absorbers for photovoltaic applications. It is important to note that only after ten years of efforts, hybrid organic–inorganic halide perovskite-based solar cells have reached 25.2% PCE with the certified world record [10], which is over 80% of its Shockley–Queisser limit (SQL). Moreover, the unique optoelectrical properties of the halide perovskites have facilitated advances not only in solar cells [11,12], but also in a large number of emerging applications such as memories [13,14], photodetectors [15,16], X-ray detectors [17,18], and light-emitting diodes (LEDs) [19,20], some of which are even compatible and going above the commercial level of performance.

Interestingly, in comparison with polycrystalline phase thin films, single crystal halide perovskite materials show superior properties in various optoelectronic applications such as solar cells, photodetectors, and light-emitting diodes. Perovskite single crystals with higher crystallinity have larger grains, which lead to lower trap density, higher stability, broader light absorption spectra, and better optoelectrical properties [8,21–24] that overcome the limitation of polycrystalline thin film. Theoretically, single crystal-based devices exhibit better performance [8]. Thus, high-quality perovskite single crystals that provide a good platform to investigate the intrinsic properties of perovskite [25] as well as higher potential of efficient photovoltaic applications over polycrystalline thin films are highly desirable. In a realistic context, however, the halide perovskite single crystal-based solar cells still lag far behind their thin film-based counterparts for several reasons. The inefficient carrier transport and collection behaviour due to the mismatch of the relatively short diffusion length and large thickness limit the application of single crystals for high-performance devices in a vertical structure. There are other obstacles like a defective surface with high trap density and the weak interaction with the functional layers, which causes interfacial voids hindering the progress. Recently, a 20 μm -thick MAPbI₃ (MA⁺: methylammonium, CH₃NH₃⁺) monocrystalline made by space-limited low-temperature crystallisation was fabricated into inverted-structure solar cells with a PCE of 21.9% [26], thus narrowing the gap between the single crystals and polycrystalline thin films. The confined thickness increases the chances for carriers to be collected at electrodes, which can be controlled as small as tens-of-nm scale to hundreds-of- μm scale [27–31]. The low-temperature crystallisation process diminishes the escape of MA⁺ to reduce MA⁺ vacancies. It offers more opportunities to enhance the fill factor (FF) and get closer to the SQL.

In this review, an overview of the recent progress on halide perovskite single crystals will be addressed including fundamental properties, synthesis methods of high-quality single crystals, and their applications. In particular, single crystal-based optoelectronic device applications will be reviewed with the newly developed single crystalline thin films and device fabrication methods. Importantly, critical discussion on the existing challenges and corresponding solutions will shed significant insight into exploring strategic approaches to further promote the research of single crystals and their device applications.

2. Properties of Single Crystals

Perovskite is a group of materials that have the general molecular structure of ABX₃, where a variety of elements can be embedded into A, B, and X. For hybrid organic–inorganic lead halide perovskite, A stands for organic groups like MA⁺ and FA⁺ (FA⁺: formamidinium, CH(NH₂)₂⁺), B is occupied Pb²⁺, and X is occupied by halide. The Goldschmidt tolerance factor t is an indicator of stability and distortion of the halide perovskite crystal structure, which is given by $t = (r_A + r_B) / [\sqrt{2}(r_B + r_X)]$, where r_A , r_B , and r_X are the ionic radii of ion A, B, and X, respectively. As mentioned, hybrid organic–inorganic halide perovskite has both organic and inorganic metal components that combine the advantages of high solubility in various organic solvents and efficient carrier transportation with the inorganic frame, indicating the wet processability and good electrical properties. Theoretically, to assure a stable structure, t should be within a specific range. For different compositions with different t , the crystal structure changes among the cubic phase, tetragonal phase, or orthorhombic phase [32]. The tolerance

factor t lies within 0.9 to 1, when the perovskite has an ideal 3D cubic structure. The value of t reaches 1, when the crystal structure is in the most stable state. The value of t is higher than 1, when cation A is much larger than cation B, and a layered 2D structure of the Ruddlesden–Popper phase is formed. When cation A is smaller than cation B, it tends to form an orthorhombic, rhombohedral, or tetragonal structure with t in the range of 0.7 to 0.9 [33]. Figure 1 gives the typical 3D perovskite crystal structure of MAPbI₃, the most studied hybrid organic–inorganic halide perovskite, where Pb²⁺ coordinates with six neighbouring iodide ions, forming corner-sharing [PbI₆]^{4−} octahedra, while the freely rotating MA⁺ is located at the centre of eight [PbI₆]^{4−} octahedra and surrounded by 12 iodide ions. The special structure of BX₆ octahedra mostly contributes to these unique optoelectrical properties.

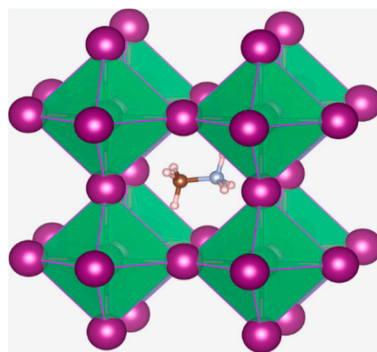


Figure 1. Crystal structure of MAPbI₃. The MA⁺ cation is located at the centre of the structure, while surrounded by eight corner-sharing [PbI₆]^{4−} octahedra. Reproduced with permission from [34]. Copyright 2015, Springer Nature.

By tuning the composition and t factor, the characteristics of perovskite vary a lot, providing more opportunities to achieve target parameters. Mixed organic groups [35–37], mixed halides [35,38,39], and alloying inorganic cations with organic cations [40] were all reported to have an effect on the tuning properties. It is because of the variable chemical composition and crystal structure that perovskite has excellent photoelectric properties and broad application prospects. Specifically, tunable bandgap is one of the features of perovskite. The replacement of organic cation A shows a significant effect on the tolerance factor t and the crystal structure, as mentioned. The bandgap experiences change with different cations. Perovskite with larger A cations tends to have a wider bandgap due to the interplay of spin–orbit coupling and octahedra tilting [9]. More significantly, the bandgap can be tuned by changing the halide ion X. In the MAPbX₃ system, the bandgap varies when changing the X composition. It was reported that by increasing the ratio of I/Br in MAPb(I_{1−x}Br_x)₃, the bandgap can be tuned from 2.28 eV (Br[−] only) to 1.58 eV (I[−] only) [41]. A partial replacement of I[−] by Br[−] can slightly increase the bandgap, while still maintain the crystal structure.

Interestingly, even different facets of one single crystal show different properties. This is called the anisotropy phenomenon. It was reported that the (100) and (112) facets of the MAPbI₃ single crystal exhibited different ion migration behaviour and defect status [42]. The I[−] vacancy dominated (100) facet followed n-type behaviour, while the (112) facet displayed p-type behaviour with MA⁺ and Pb²⁺ dominance. Another work revealed that stronger ion migration occurred in the (002) facet of MAPbI₃ single crystals [43]. The anisotropy phenomenon gives an idea of facet engineering for high-performance applications on favourable facets of single crystals.

Most of the perovskite applications are fabricated based on polycrystalline thin films with several hundred of nanometres. Commonly, vacuum evaporation and solution processing are used to deposit thin films [44]. The quality of thin films largely depends on the fabrication process. Efforts have been made to fabricate conformal and pinhole-free high-quality films. Apart from the technical factor, polycrystalline thin films inherently have low crystallinity, which is reflected in the presence of a large number of grain boundaries and defects that negatively affects the performance of solar cells in terms of

PCE and stability. Grain boundary is the interface between two crystallites. It was reported that faster nonradiative recombination and photoluminescence (PL) quenching favourably takes place at the grain boundaries [45], ascribing to faster ion migration and accumulation [46]. Defects are the interruptions of regular patterns. The lattice around the defect is distorted and the periodic potential field is damaged. This kind of deformation will create an energy level in the electronic band. Deep-level defects can act as recombination centres where carriers are captured, and non-radiative recombination happens, resulting in free carrier loss. Generally, grain boundaries and defects are regarded as fatal, and decrease semiconductor properties. Compared with polycrystalline thin films, single crystals have much better crystallinity. The spontaneous crystallisation process ensures single crystals with continuous and rigid crystal lattices [47], so the structure distortion and grain boundaries rarely exist in single crystals as well as fewer defects. High-quality single crystals exhibit several orders of magnitudes lower (10^9 – 10^{11} cm^{−3}) defect density than that of thin films (10^{16} – 10^{18} cm^{−3}) [5,48], which is comparable to high crystallinity Si semiconductors [5], suggesting a lower possibility of carrier trapping and recombination. The difference in trap density is also observed in silicon. Disorder in the structure leads to localisation of the states, which appear as band tails within the band gap. These tails are usually described with an exponential density of states [49]. For hybrid organic–inorganic perovskite single crystals, the absence of grain boundaries and high crystallinity in the bulk crystal contribute most to the low trap density. This also allows single crystals to have higher carrier mobility, longer diffusion length, and wider light absorption spectra [21]. Specifically, the MAPbI₃ single crystal was reported to have a surprisingly high carrier diffusion length exceeding 175 μm [4] and a carrier lifetime exceeding 15 μs [50]. An extra-long diffusion length exceeding 380 μm under 1 sun illumination was reported for hybrid CH₃NH₃PbI₃Cl_x single crystals [51]. Regarding the thin films, a much shorter diffusion length of ~1.7 μm for electrons and up to ~6.3 μm for holes was directly observed [52], and the lifetime was dependent on film thickness and the surface defects [53], for which the value varied from 2.8 ns [52] to over 140 ns [54]. This huge difference means that carriers can stay untrapped and unrecombined for a longer time and distance to move to the electrodes in single crystals. Moreover, single crystals exhibit wider absorption spectra and high light absorbance [4,55–58]. The Snaith group reported the thickness-dependent light absorptance of MAPbI₃ thin films where about 90% of the incident light could be absorbed with films with a 300–400 nm thickness [59]. The light absorptance further increased to over 99% when the film thickness was over 600 nm. Furthermore, the absorption cut-off of single crystals was located at 850 nm, showing a red shift compared to 800 nm of polycrystalline thin films. It is noteworthy that the perovskite single crystal is an ideal platform to investigate the intrinsic nature of this material, especially for carrier dynamic and mobility [32] because of the superior properties and large dimensions.

Large dimension brings convenience to an intrinsic nature study; however, it also brings challenges to the direct application of single crystals in high performance photovoltaic devices. Though the large thickness can increase the light absorption, it is detrimental for charge separation and collection, which causes a decrease in the external quantum efficiency and thus hinders device performance. To be more specific, photovoltaic applications like solar cells require light-induced carriers to be captured by electrodes to generate voltage across the solar cell and external current. Generally, single crystals are grown in bulk, with thicknesses of several millimetres that far surpasses the carrier diffusion length, while for polycrystalline thin films, it is hundreds of nanometres, so it is much easier for carriers to transport across the cell. Another obstacle is the difficulty of incorporating multilayer devices because the majority of single crystals are free-standing and not attached to any substrate. Therefore, large-area and thin single crystals are highly desired for device fabrications. Recently, researchers have been trying to use the space-confined crystallisation method to grow a single-crystalline thin film with thicknesses ranging from tens of nanometres [27] to hundreds of micrometres [60–62]. Using this method, thin single crystalline thin films have been successfully made into devices with vertical structures. A PCE of 21.09% with a maximum FF of 84.3% was achieved by an inverted structural device ITO (indium tin oxide)/poly(triarylamine) (PTAA)/MAPbI₃ single crystal/C60/bathocuproine (BCP)/copper (Cu) based

on a ~20 μm -thick MAPbI_3 single crystal, which performed better than the polycrystalline devices with the same structure (~19% in PCE) [63]. Most recently, a new record of 21.93% was made by the same group using the modified crystallisation process. Remarkable enhancement in the open circuit voltage (V_{OC}) from 1.08 V (controlled sample) to 1.15 V was observed. The accelerated progress of single-crystalline thin films encourages competition with the polycrystalline counterpart. The chances of surpassing lie in the further improvement of crystal quality and the surface engineering of the device.

3. Synthesis Methods of Perovskite Single Crystals

In the middle of the twentieth century, scientists started synthesizing perovskite single crystals. In 2015, Zhipeng Lian and coworkers synthesised MAPbI_3 single crystals by the bottom-seeded solution growth (BSSG) method, and first fabricated single-crystal based photodetectors on the (100) facet [64], where the superiority of the perovskite single crystals was revealed. Compared with polycrystalline thin film photodetectors, their devices showed a 10^2 times higher responsivity and 10^3 times higher response speed, greatly encouraging the exploration of single crystals.

To obtain high quality single crystals, several solution-processed crystallisation methods have been developed, mainly in three categories of the antisolvent vapor-assisted crystallisation (AVC) method, solution temperature-lowering (STL) method, and inverse temperature crystallisation (ITC) method. The fundamental mechanisms of these methods are to create supersaturation in the precursor, modulate the solubility, and induce crystallisation. Researchers are keeping the optimizing crystallisation process toward a low temperature-process and controlled nucleation based on these methods to obtain larger-sized high-quality single crystals.

3.1. Antisolvent Vapor-Assisted Crystallisation (AVC) Method

During perovskite thin film deposition, antisolvents are commonly used to accelerate crystallisation and improve film quality [65,66]. The mechanism is to use the large solubility difference of perovskite in different solvents. For common solvents like dimethyl sulfoxide (DMSO), dimethylformamide (DMF), and gamma-butyrolactone (GBL), MAPbI_3 dissolves well, while in antisolvents like chlorobenzene (PhCl), diethyl ether (Et_2O), and dichloromethane (DCM), MAPbI_3 shows low solubility. In the process of thin film deposition, the perovskite precursor is firstly spin coated on substrates followed immediately by the deposition of the antisolvent. Antisolvents induce fast nucleation and crystallisation, increasing the grain sizes and film uniformity. In addition to low solubility, the antisolvent is required to be highly volatile and can dissolve well in the chosen solvent to make sure the efficient diffusion into the solvent. Based on this strategy, Bakr's group first developed the AVC method to grow single crystals [5]; Figure 2a illustrates the AVC process for single crystals. The same molar ratio of MAI and PbI_2 are dissolved in solvent gamma-butyrolactone (GBL) to get the precursor solution. In a closed environment, the open vial containing precursor solution is covered with a large vessel with antisolvent dichloromethane (DCM). When the vapor of the antisolvent mixes with the precursor solution, the solubility of the target crystals reduces, thus crystallisation is promoted [55]. Crystals slowly grow along with the gradual diffusion of the antisolvent. The MAPbBr_3 and MAPbI_3 crystals shown in Figure 2b were obtained within one week of crystallisation. Figure 2c shows a modified AVC setup where a temperature controller and a flow controller are used to ensure a stable environment and continuous antisolvent diffusion for high-quality and large single crystals [67]. A large MAPbBr_3 single crystal over 50 mm in size was grown with this modified method (Figure 2d) after over-15-day synthesis. Compared with conventional temperature-tuning crystallisation methods, the AVC method avoids the temperature-dependent phase transitions, and the disturbance of convective currents; it also prevents the potential lattice disorder due to the solvation of MA^+ during the crystal growth. However, the crystal growth rate is relatively low.

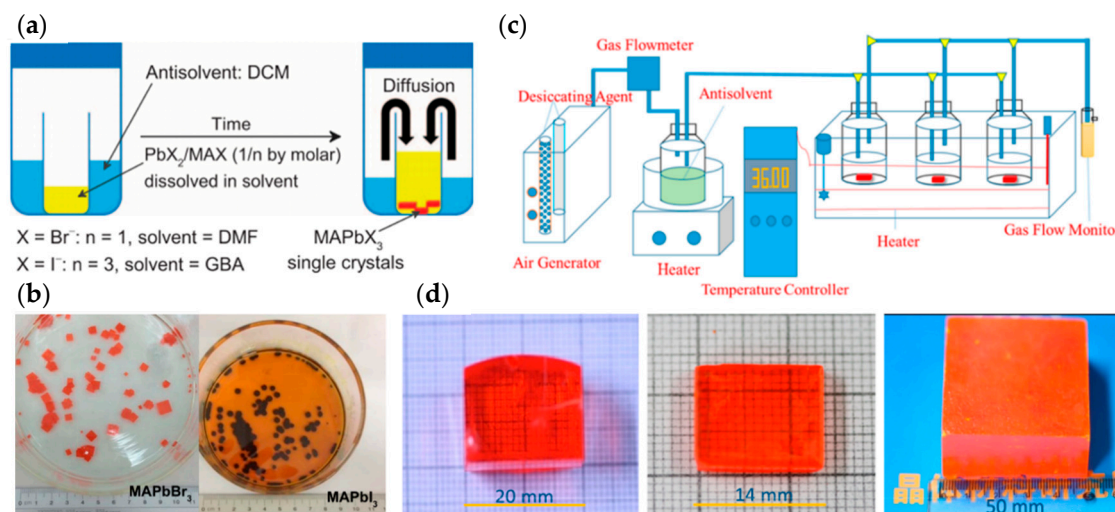


Figure 2. Schematic diagrams of AVC method and images of the as-obtained single crystals. (a) Schematic diagram of the uncontrolled AVC method, and (b) photographs of the as-grown MAPbBr₃ and MAPbI₃ single crystals. Reproduced with permission from [5]. Copyright 2015, The American Association for the Advancement of Science. (c) Schematic diagram of the settled temperature and controlled antisolvent diffusion setup for the AVC method and (d) photographs of the as-grown MAPbBr₃ single crystals in different sizes, of which the largest size exceeds 50 mm. Reproduced with permission from [67]. Copyright 2018, American Chemical Society.

3.2. Solution Temperature-Lowering (STL) Method

The STL method is a classic crystallisation method that creates supersaturation by lowering the temperature. It is suitable to grow perovskite in the HX-based precursor solution, because its solubility greatly decreases as the temperature goes down. Figure 3a gives the solubility curve of MAPbI₃ in HI solution. Briefly, Pb(CH₃COOH)₂·3H₂O and MAI are dissolved in a HI aqueous solution at 60 °C, then the temperature is cooled to 45 °C at a slow rate of 0.1–0.5 °C per hour [68]. Consequently, single crystals with a 10 mm size can be harvested [69] (Figure 3b). STL method was further optimised by fixing seed crystals in different positions in the vessel with the top seeded solution growth (TSSG) method and the bottom seeded solution growth (BSSG) method. Figure 3c,d illustrates the setup of the two methods. For BSSG, first, small seed crystals with a millimetre scale were obtained by the STL method. Nice seeds were picked out and put in the bottom of the vial with fresh precursor for further growth. This step is repeated until the targeted size was attained. For TSSG, nice small seeds were fixed on a substrate that is immersed in the top half of the precursor. The bottom half of the vial containing precursor and seed crystals is heated in an oil bath while the top half is air cooled to remove the heat and create a temperature gradient [4]. Low temperature at the top induces the crystallisation, at the same time, the bottom continuously provides ions by convection [32]. Large size single crystals can be obtained by STL under the strict control of temperature, but the growth rate is relatively low (2 mm per day). Irregular crystals and MA₄PbI₆·2H₂O by-products will be formed if the temperature drops too fast or decreases below 40 °C. Formic acid was reported to be effective in accelerating the STL crystallisation and promoting a higher quality of MAPbI₃ single crystals [70]. A crystal of 9 mm in length was obtained by 3-day direct growth without seed.

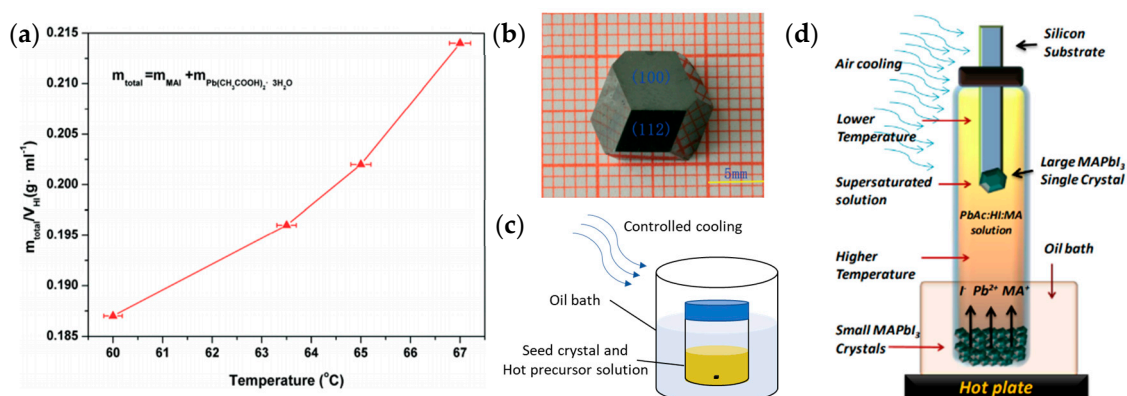


Figure 3. The mechanism and illustrations of STL method. (a) Solubility curve of MAPbI₃ in HI solution, and (b) image of MAPbI₃ grown by STL method oriented to exhibit its natural facets (100) and (112). Reproduced from [69] with permission from The Royal Society of Chemistry, 2015. Schematic diagrams of (c) BSSG method and (d) TSSG method. Reproduced with permission from [4]. Copyright 2015, The American Association for the Advancement of Science.

3.3. Inverse Temperature Crystallisation (ITC) Method

The ITC method was first proposed in 2015 by Bakr's group, and is now the most commonly used method for lead halide perovskite single crystal synthesis [56,71]. In certain solvents, the solubility of perovskite shows retrograde behaviour, which decreases as the temperature increases, and keeping the precursor at high temperature can promote crystallisation. For MAPbI₃, MAPbCl₃ and MAPbBr₃, GBL, DMSO, and DMF are suitable solvents in the ITC method, respectively. The solubility of perovskite in the corresponding solvent for the ITC method is illustrated in Figure 4a–d. The mechanism is that, at low temperature, the perovskite forms complexes with the solvent, exhibiting high solubility. As the temperature increases, the bonds break, perovskite molecules are freed, and the solubility drops. This method is applied to formamidinium and methylammonium lead halide perovskites [23,71] as well as mixed halide perovskite [72]. The synthesis procedure of the ITC method is quite simple. Taking the crystallisation of MAPbI₃ single crystals as an example, 1 M of PbI₂ and MAI are dissolved in GBL at a 45 °C to form a saturated precursor, which is then heated to 80–130 °C. The precursor is kept at a specific temperature for several hours, and MAPbI₃ on a millimetre scale can be obtained. Repeated seeded growth is conducted to harvest large crystals. Figure 4e gives an illustration of the ITC method. The growth rate of MAPbI₃ was calculated to be 3 mm³h^{−1} for the first hour and exponentially increased for the following hours (Figure 4f), one order of magnitude faster than other methods [23,69]. ITC is simple to operate and fast in growth, but the growth rate is hard to control, consequently inducing more defects.

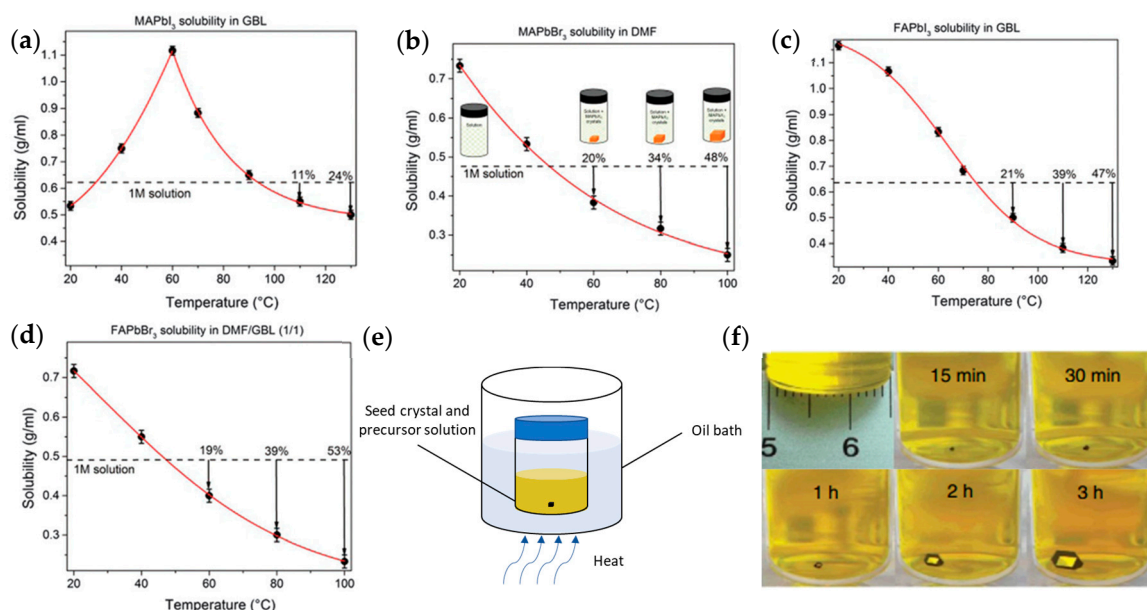


Figure 4. Temperature-dependent solubility curves of (a) MAPbI₃ in GBL, (b) MAPbBr₃ in DMF, (c) FAPbI₃ in GBL, and (d) FAPbBr₃ in DMF:GBL (1:1 in volume), showing yield at different temperatures. Reproduced from [71] with permission from The Royal Society of Chemistry, 2015. (e) Schematic diagram of the ITC method where the precursor vial is immersed in oil bath, heated, and kept at high temperature for crystallisation. (f) Photographs of the growth of a MAPbI₃ crystal at different time intervals. Reproduced with permission from [23]. Copyright 2015, Springer Nature.

4. Optoelectronic Applications of Perovskite Single Crystals

Perovskite, as one of the most promising candidates of next-generation semiconductor materials, has demonstrated a wide range of device applications. As the most widely studied application of perovskite, the perovskite single junction solar cell has achieved a PCE over 80% of the theoretical value. Researchers are now focusing on modifying the interfaces between the perovskite with electron transport layers and hole transport layers. On the other hand, the development of another potential application, perovskite photodetectors and X-ray detectors, is still in its early stage. Optimisations on single crystals with low trap density and high crystallinity are still desirable. As mentioned, the exploration of high-performance photodetectors with perovskite single crystals is quite encouraging. Ye reported a perovskite photodetector exhibiting a high detectivity of 1.8×10^{15} Jones and a response time of 68.9 μ s with high quality cuboid MAPbI₃ single crystals. The X-ray detector made with the same material showed a sensitivity of 969.9 μ C Gy⁻¹cm⁻² under -1 V bias, which went as high up to 6218 μ C Gy⁻¹cm⁻² under -13 V bias. In the following part, some representative applications are summarised.

4.1. Perovskite Single Crystal for Solar Cells

Efficient carrier transport plays a dominant role in the performance of solar cells, which requires carriers to travel across the light-absorb layer to the electrodes. For bulk single crystals, the mm-scale thickness did not match the μ m-scale carrier diffusion length, leading to incompatibility with the vertically multi-layer solar cell structure. Furthermore, free-standing bulk single crystals have a small aspect ratio that is not suitable for device fabrications. Therefore, controlling the thickness of single crystals down to at least the μ m-scale is one of the prerequisites for high-performance solar cells. Efforts have been made to grow large-area single crystals directly on substrates. Here, the major fabrication methods of single-crystalline thin films and solar cell applications are summarised.

The top-down method is a universal and easily applicable method to prepare single-crystalline thin films, especially large-area thin films, from bulk single crystals by mechanical slicing [57] and

grinding [73]. Liu et al. reported the fabrication of large-area single-crystalline thin films from a series of single halide and $\text{MAPb}(\text{Cl}_x\text{Br}_{1-x})_3$ and $\text{MAPb}(\text{Br}_y\text{I}_{1-y})_3$ mixed halide perovskite bulk single crystals by diamond-wire sawing [57]. They optimised the coolant solution, the sawing speed, and the feeding rate of the slicing machine to cut a $113 \text{ mm} \times 58 \text{ mm} \times 52 \text{ mm}$ -large MAPbI_3 single crystal into wafers with thicknesses of 190, 380, and 570 μm . The as-cut wafers were characterised to have a high quality with a low trap density of $2.1 \times 10^8 \text{ cm}^{-3}$, a low hole concentration of $6.1 \times 10^9 \text{ cm}^{-3}$, a high carrier mobility of $41 \text{ cm}^2\text{V}^{-1}\text{s}^{-1}$, and high absorption onset of 910 nm. Wafers were made into solar cells with an Au/ITO/Spiro-MeOTAD/perovskite-wafer/PCBM/LiF/Ag/Au structure. The best device had a open circuit voltage (V_{OC}) of 1.15 V and short current density (J_{SC}) of 20.02 mAcm^{-2} , and interestingly, minor hysteresis between the reverse scan and forward scan. However, the efficiency was as low as 4%. It is speculated that the slicing process can cause damage on the wafer surface including high roughness and surface defects. Oxygen and moisture could intrude on the surface during the slicing process, resulting in surface degradation, at the same time, coolant solution could cause partial dissolution of the crystal. Moreover, top-down method can hardly produce wafers with thicknesses below 50 μm , which is still too thick for efficient carrier transport. The poor contact between the HTL, ETL, and the wafer could be another obstacle for high performance.

Later, a universal top-down approach that combined mechanical slicing and wet etching was developed by Yan's group [74]. Large thick single crystals were first wire-cut into wafers in 200- μm thicknesses. The thin wafers were then immersed in unsaturated mother liquor for wet etching by controlling the immersion conditions (time, temperature, and concentration), and the thickness of the wafers could be reduced to as low as 15 μm , as shown in Figure ??a. The combined process preserves the surface properties of the original large single crystal without obvious degradation and maintains the crystallinity, but still, the thickness of the thin wafers cannot be reduced below micron-scale and the thin wafers had relatively small area. They did not report the application of solar cells in this literature. However, this method is promising to synthesize single-crystalline thin films without damaging the surface properties for high-performance solar cells.

The cavitation-triggered asymmetrical crystallisation (CTAC) strategy was first reported by Bakr's group for the growth of monocrystalline MAPbBr_3 films on various substrates including silicon wafers, ITO-coated glass, FTO-coated (FTO: fluorine-doped tin oxide) glass, and sputter-coated metal on silicon [75]. Ultrasonic pulse with antisolvent vapor diffusion was introduced to a low supersaturated precursor to generate cavities, where the formation and collapse can release energy to overcome the nucleation barrier and promote symmetric crystal growth near the substrate by high-speed fluid jets, as demonstrated in Figure ??b. By regulating the rate and time, the film thickness was controlled from one up to several tens of micrometres, however, the larger the thickness, the weaker the performance. Their ETL and HTL-free devices of ITO/ MAPbBr_3 (4 μm)/Au had a PCE of over 5%, which was improved to 6.5% with a single p-n-junction-based structure of FTO/ TiO_2 / MAPbBr_3 (1 μm)/Au that exhibited a high V_{OC} of 1.4 V. The dark and illuminated J-V curves for the two samples are as in Figure ??c,d. This work gives an insight of the design of rational device structures.

Breakthroughs on single-crystal solar cells were attained using space-confined solution-process method. It was first developed by Liu et al. to fabricate single-crystalline thin film photodetector devices using an ultrathin geometry-defined dynamic-flow reaction system [76], as shown in Figure ??e. Substrates are separated by different spacers; a peristaltic pump continuously provides fresh precursor with dynamic flow into the middle layer. Single crystalline wafers (thinnest to 150 μm) are obtained in the interspace. Later in 2017, Huang and co-workers reported MAPbI_3 single crystal growth on poly(triarylamine) (PTAA) coated ITO substrates for high-performance solar cells [8]. The hydrophobicity of PTAA weakens the solvent-substrate interaction, thus promoting the solvent diffusion, which benefits the in-plane crystallisation, as shown in Figure 6a. They studied thickness-dependent performance and concluded that, theoretically, single crystals with a 200 μm thickness can reach the highest PCE (Figure 6b), however, from the experiment, the 10 μm -thick crystal displayed the best performance. This is due to the inconsistent of the carrier diffusion length

of the bulk single crystal and the single-crystalline thin film. The hole and electron diffusion length were 24.7 and 13.6 μm , respectively, in this report, far shorter than those reported values of the bulk crystals. The resultant devices of ITO/PTAA/MAPbI₃ (10 μm)/phenyl-C61-butyric acid methyl ester (PCBM)/C60/bathocuproine (BCP)/copper (Cu) had the best PCE of 16.1%, which was increased to 17.8% with a J_{SC} of 21.0 mA cm^{-2} , a V_{OC} of 1.08 V, and a FF of 78.6% by surface passivation of MAI. Later in 2019, Bakr's group fabricated a solar cell with a similar method, but was conducted in a N₂-filled environment, which had a J_{SC} of 23.46 mA cm^{-2} , a V_{OC} of 1.076 V, a FF of 83.5%, and a PCE of 21.09% [63]. Figure 6c illustrates the cell structure and band energy of each layer of ITO/PTAA/MAPbI₃ (20 μm)/C60/bathocuproine (BCP)/Cu. It was speculated that the easy-to-oxidize I[−] may result in I₃[−] trimers that form deep-level defects [77,78], which the N₂ environment can prevent. Most recently, a new record of a PCE of 21.93% with a J_{SC} of 23.68 mA cm^{-2} , a V_{OC} of 1.144 V, and a FF of 81% was made by Bakr's group using the same device configuration [26]. They optimised the composition of the precursor solvent to a solvent mixture of propylene carbonate (PC) and γ -butyrolactone (GBL) for low-temperature crystallisation for high-quality single crystal thin film. The addition of PC reduced 45% of the solubility of MAPbI₃, but still kept the retrograde solubility behaviour, so that a single crystal could be obtained at the lower temperature at 90 °C, which alleviated the escape of MAI from the crystal lattice (Figure 6d,e), consequently, improving crystallinity and performance. An improvement of over 1% on PCE was achieved by lowering the crystallisation temperature, as shown in Figure 6f.

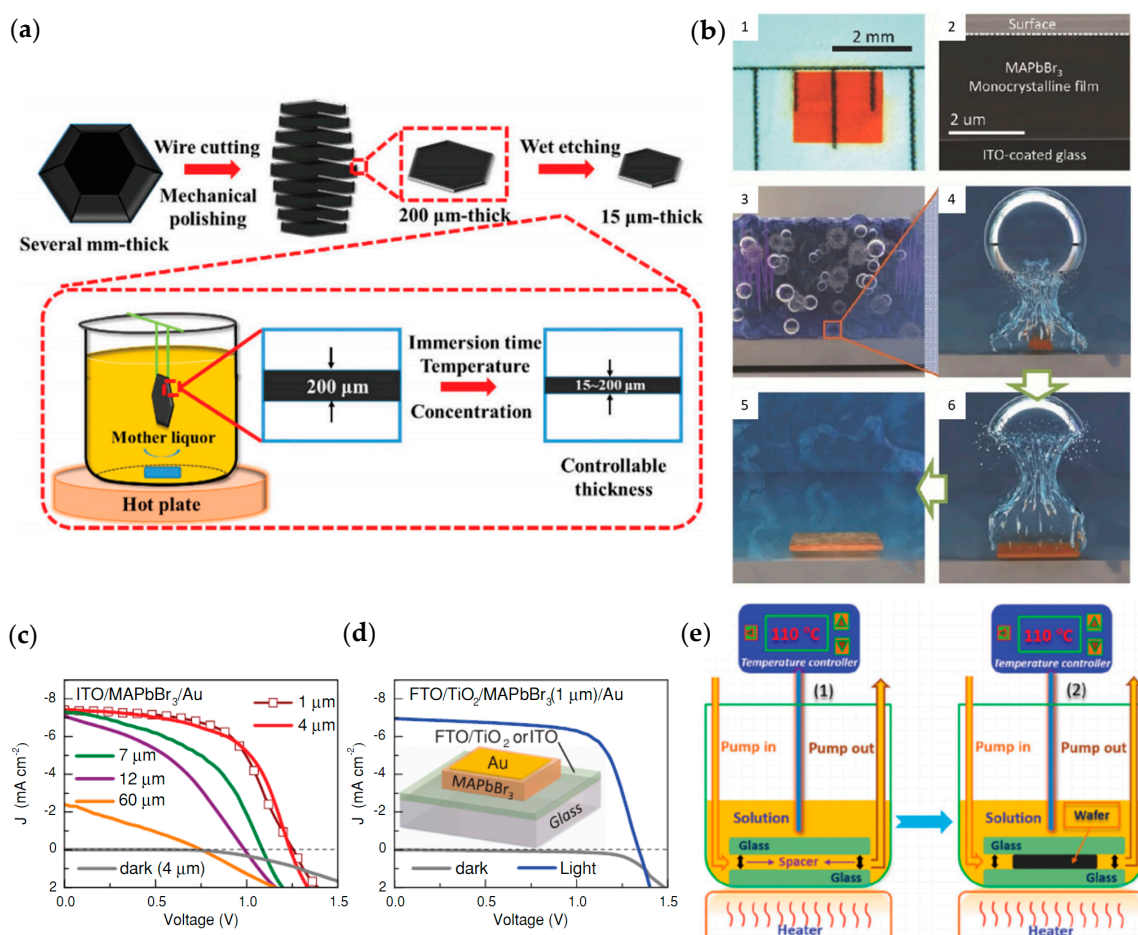


Figure 5. Schematic diagrams of top-down, CTAC and space-confined solution process methods for synthesis of perovskite single-crystalline thin films, and the application of solar cells. (a) Schematic diagram of a thickness-controllable top-down method that combines mechanical slicing and wet etching processes. Reproduced from [74] with permission from The Royal Society of Chemistry, 2018. (b) Images and illustrations of CTAC method: 1, The optical image and 2, cross-section scanning electron microscope

(SEM) image of the monocrystalline film; 3–6, illustrations of the cavity formation and collapse of the CTAC mechanism on a microscopic scale; dark and illuminated J–V curves of (c) ITO-based and (d) FTO/TiO₂-based monocrystalline solar cells, respectively, the inset depicts an illustration of the device architecture. Reproduced with permission from [75]. Copyright 2016, WILEY-VCH. (e) Schematic diagrams of the ultrathin geometry-defined dynamic-flow reaction system. Two flat glass slides are separated apart by two spacers (Si wafers, stainless-steel foils, wires, etc.) to form a microreactor in which the single crystal wafer is formed. Reproduced with permission from [76]. Copyright 2016, WILEY-VCH.

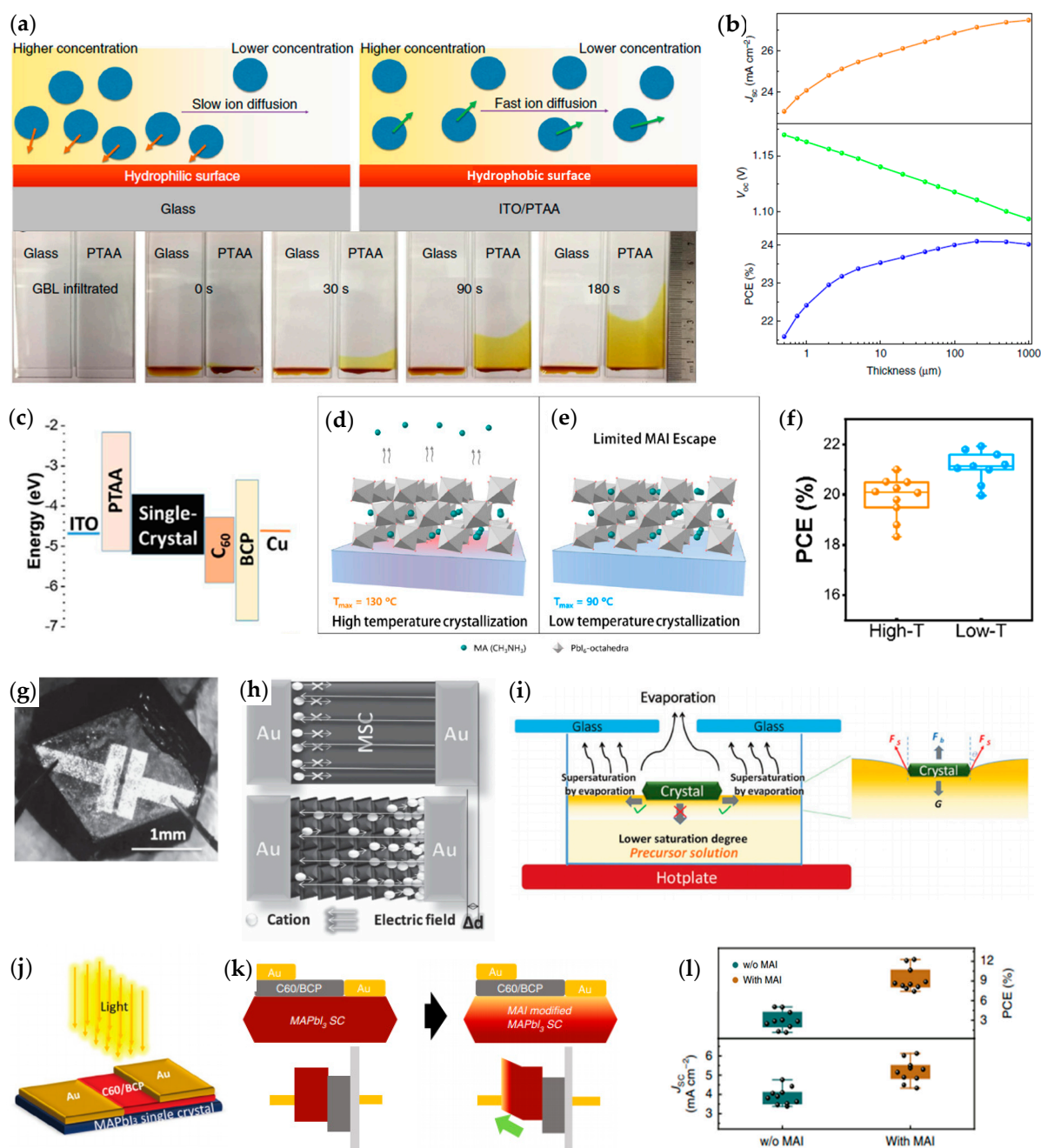


Figure 6. Schematic diagrams of high-performance single-crystal solar cells and illustrations of lateral-structure single-crystal solar cells. (a) Schematic diagrams of ion diffusion on hydrophilic and hydrophobic substrates, and photographs of the diffusion process of methylammonium lead triiodide (MAPbI₃) precursor solution in the confined gaps after different durations using hydrophilic glass and hydrophobic PTAA-covered ITO substrates, and (b) the calculated ideal dependence of J_{sc} , V_{oc} , and PCE of the single crystal solar cells on the thickness of the thin single crystals. Adapted with permission from [8]. Copyright 2017, Springer Nature. (c) Energy-level diagram for single crystal solar cell. Reproduced with permission from [63]. Copyright 2019, American Chemical Society. Further permissions related to the material excerpted should be directed to the ACS. Schematic illustration of methylammonium iodide escape from MAPbI₃ single-crystal films at (d) high-temperature (High-T) and (e) low-temperature (Low-T) crystallisation. (f) Statistical comparison of the PCE for 10 devices including measured under 1 sun illumination. Reproduced with permission from [26]. Copyright 2020, American Chemical Society. (g) An image of MAPbI₃ lateral structure single-crystal device, and (h) scheme of electromechanical strain induced grain boundaries and ions migration in MAPbI₃ single crystals. Reproduced with permission from [68]. Copyright 2016, WILEY-VCH. (i) Scheme of surface tension assisted growth mechanism; (j) scheme of MAPbI₃ crystal-wafer lateral-structure solar cell device. Reproduced with permission from [79]. Copyright 2019, WILEY-VCH. (k) Schematic diagram of device structures and energy levels for lateral solar cell based on single crystal without and with MAI treatment and (l) performance data before and after MAI treatment (0.25 sun) including J_{sc} and PCE. Reproduced with permission from [30]. Copyright 2020, Springer Nature.

There are also some cases of lateral-structure solar cells. Dong and coworkers simply deposited two symmetrical gold electrodes with a spacing of 50 μm on the top surface of a single crystal, forming an Au/MAPbI₃/Au structure, and this device is shown in Figure 6g. When a high electrical field of 1 $\text{V}\mu\text{m}^{-1}$ was applied in the device, reversible shape changing was observed, which was likely due to the slipping between the weakly bonded (100) planes to relieve the accumulated strain. The slipping induced defect and grain boundaries in the crystal act as a high-speed channel for ion migration, resulting in self-doping, thus, after the electrical poling, the symmetry of the device was broken into a lateral p-i-n structure solar cell. This process is illustrated in Figure 6h. The device exhibited a J_{sc} of 2.28 mA cm^{-2} and a V_{oc} of 0.82 V under 0.25 sun. The PCE was hindered by the poling-induced high trap density as 1.88%. Later in 2019, the same group used the surface tension assisted growth method to synthesize single-crystalline thin films with a large aspect ratio and fabricate lateral-structure solar cells [79]. As illustrated in Figure 6i, in brief, by controlling the solvent evaporation of the precursor, nuclei favourably form at the centre of the solution top surface due to fast evaporation at the centre and float at the air–solution interface with the support from surface tension. Then, the thin crystals grow along the lateral direction along with evaporation. The as-grown wafers have a lateral size in centimetres and a thickness of tens of micrometres as well as wider light absorbance and prolonged carrier lifetime. The best lateral solar cell of Au/MAPbI₃/C60/BCP/Au had a J_{sc} of 5.06 mA cm^{-2} , V_{oc} of 0.66 V, FF of 44%, and PCE of 5.9% under 0.25 sun without poling treatment (Figure 6j). For the lateral-structure solar cells, surface treatment is highly desired to reduce the surface trap density because surface defects would significantly limit the carrier diffusion length at the near surface region. The carrier diffusion length is expected to be over 50 μm , as this is the normal gap between two electrodes. Song reported that surface passivation by MAI on the MAPbI₃ single crystal is effective in improving the solar cell efficiency, which increases the surface potential and encourages better energy band alignment of the device, as shown in Figure 6k. The PCE of devices based on the passivated single crystal exceeded 11% (Figure 6l), and the operation stability was enhanced to 200 h without degradation.

Though the PCE of the single-crystal solar cell was improved to 21.93%, there is still a huge gap between the single-crystal devices and polycrystalline counterparts (25.2%). It is worth noting that single-crystal solar cells still suffer from the significant surface trap density, despite the low trap density

in the bulk. Moreover, the lattice mismatching between the perovskite and deposited layer requires optimisation by interface engineering.

4.2. Perovskite Single Crystals for Photodetectors

A photodetector is a sensor of light that presents in a large variety of equipment for light imaging sensing, process control, and security purposes. It converts an indecipherable light signal into an electrical signal with a semiconductor that displays the photovoltaic effect or photoconductivity with an external voltage. The key parameters that describe the performance of a photodetector are dark current density (J_d), external quantum efficiency (EQE), responsivity (R), specific detectivity (D^*), linear dynamic range (LDR), and response speed (rise time τ_r and fall time τ_f).

Perovskite single crystal-based photodetectors feature high R and D^* for their extraordinary characteristics. In 2015, Lian first revealed the better capability of perovskite single crystals over thin films for photodetectors [64]. The centimetre-scale MAPbI₃ single crystals grown by the BSSG method were made into planar-type photodetectors on (100) facet. Simple devices with two interdigitated Au electrodes with channel width of 20 μm were fabricated, as illustrated in Figure 7a. Under the lowest detectable light intensity (2.12 nW cm^{-2}), a high R of 953 AW^{-1} and EQE of $2.22 \times 10^5\%$ were measured at 1 V bias, with a LDR of 76 dB, τ_r of 74 μs , and τ_f of 58 μs . Under a relative strong light source of 1 mWcm^{-2} , the single crystal photodetector showed 100 times higher R (Figure 7b) and EQE, and 10^3 times faster response speed than their polycrystalline-based devices. Lian's work encouraged researches to apply high-quality single crystals for high-performance photodetectors.

The carrier dynamic of perovskite makes it ideal for the light-absorb layer. The generation of the electron-hole pair happens in several picoseconds and the free carrier concentration remains high at the microsecond scale [80], while the recombination that reduces the carriers is relatively slow at several microseconds. Fast generation and low recombination assure a fast response (low τ_r and τ_f). Additionally, the carrier mobility, lifetime, and diffusion lengths of perovskite single crystals were surprisingly high. Carrier lifetime exceeding 15 μs [50] and a diffusion length exceeding 175 μm [4] were detected. This means that carriers can stay untrapped and unrecombined for an adequate time and distance to move to the electrodes. Meanwhile, the defect density in the perovskite single crystals was as low as 10^9 cm^{-3} , comparable to that of high crystallinity Si semiconductors [5], suggesting a lower possibility of carrier trapping and power loss. These properties guarantee highly efficient collection, giving rise to an outstanding photocurrent, EQE, D^* , and R. In particular, high-quality single crystals have more chances in performance breakthroughs. Ye reported MAPbI₃ single crystal-based photodetectors with an ultrahigh detectivity. High-quality crystals were obtained by modifying the ITC method by dissolving the seeds back to the precursor prior to heating up for regrowth [81]. The impurities at the surface dissolve at low temperature, so the mismatch between the nucleus and seed surface is diminished to avoid gap defect formation, thus improving crystallinity. The as-obtained cuboid MAPbI₃ single crystals had a low trap density of $1.14 \times 10^9 \text{ cm}^{-3}$. The resultant photodetectors had the best performance of R of $2.6 \times 10^4 \text{ mAW}^{-1}$, EQE of 5700%, and D^* of 1.8×10^{15} Jones under 550 nm illumination at -1 V bias. Recently, a highly sensitive photodetector with an ultra-high R of 1017.1 AW^{-1} was reported [82]. A MAPbBr₃ single crystalline thin film (2.25 μm in thickness) was integrated with a monolayer of graphene vertically. The difference in Fermi level between the two materials pushes holes from the graphene to the perovskite side and results in electron doping in the graphene side. This charge transfer induces a built-in field that helps the efficient separation of light-generated electron-hole pairs as well as suppressing carrier recombination in the perovskite layer. Figure 7c illustrates the energy band bending of the integration. At 3 V bias, the resultant photodetector (the device structure is illustrated in Figure 7d) exhibited an R of 1017.1 AW^{-1} , D^* of 2.02×10^{13} Jones and photoconductive gain of 2.37×10^3 under 532 nm illumination with an intensity of 200 mW cm^{-2} .

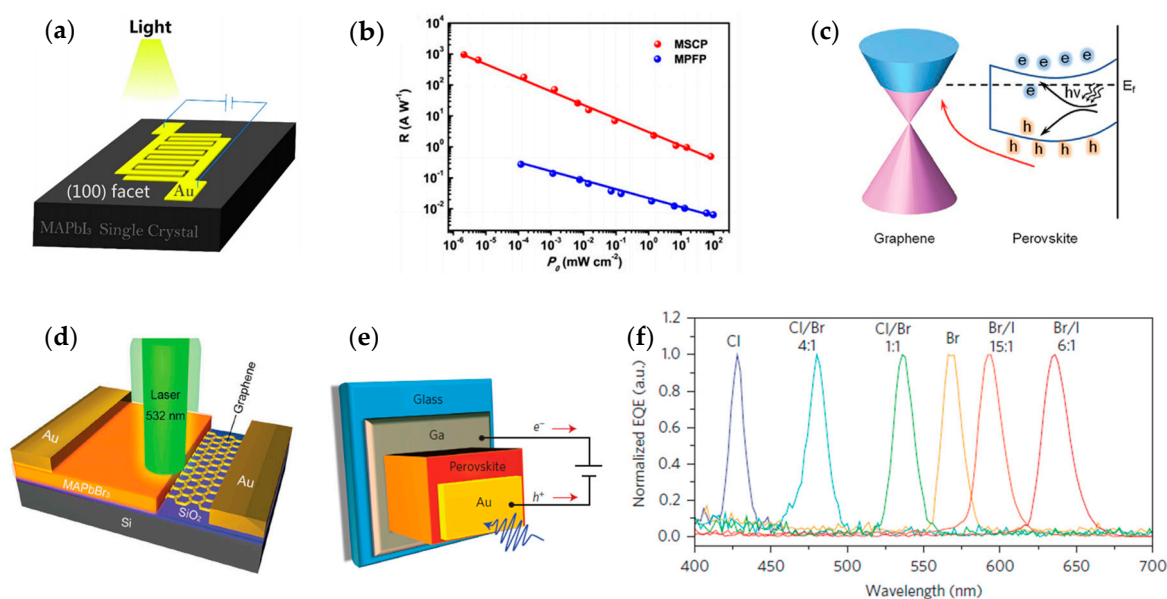


Figure 7. Schematic diagrams and the performance of single-crystal photodetectors. (a) Schematic diagram of the lateral-structure photodetector fabricated on the (100) facet of a MAPbI₃ single crystal. (b) A comparison of irradiance power-dependent R for as-fabricated single crystal-based and thin film-based photodetectors at 1 V bias. The light source was a 532 nm laser. Reproduced with permission from [64]. Copyright 2015, Springer Nature. (c) Energy band diagram of graphene–perovskite vertical device under illumination, and the (d) schematic diagram the vertical photodetector. Reproduced with permission from [82]. Copyright 2020, WILEY-VCH. (e) Schematic of device structure for narrowband photodetection. (f) Normalised EQE spectra of the perovskite single-crystal photodetectors at -1 V bias with different halide compositions of single-halide and mixed-halide, showing the tunable spectral response and ultra-narrow EQE peaks with FWHMs below 20 nm. Reproduced with permission from [15]. Copyright 2015, Springer Nature.

By tuning the composition of halide, perovskite can achieve detection in different wavelength ranges. Visible-blind UV detection was reported using a large band gap material: MAPbCl₃ single crystals [56]. MAPbBr₃ and MAPbI₃ single crystals showed strong near infrared photo responses below their optical gaps due to surface defect induced sub-gap absorption, enabling near infrared detection [83]. Fang et al. reported highly narrowband photodetectors with a vertical structure using mixed halide perovskite thick single crystals [15]. Changing the halide ratio Cl/Br and thus bandgap, the response spectral can be tuned from blue to red. Together with the “charge collection narrowing effect” and the assistance of applied voltage, response spectral with a full-width at half-maximum (FWHM) below 20 nm was achieved, as shown in Figure 7e,f. Long-wavelength light that penetrates deeper into the bulk crystal generates carriers closer to the rear electrode, which can be more easily collected, while the short-wavelength light generates carriers in the near surface region where strong surface-charge recombination happens. Therefore, charge collection in the short wavelength is limited. However, this band narrowing is at the expense of the device performances, R , and response speed due to severe carrier recombination.

2D single crystals with large organic groups and special quantum well structure also play an important part in the development of perovskite photodetectors. Wang systematically studied the effect of the number of metal halide monolayer sheets, n , on the performance of simple planer-type devices with Au/perovskite single crystal/glass, based on BA_{*n*}MA_{*n*-1}PbI_{3*n*+1} (BA⁺: butylammonium, C₄H₉NH₃⁺; $n = 1, 2, 3, 4$ and ∞) single crystals [36], as illustrated in Figure 8a. With a thinner quantum well thickness, significant reductions in J_d , τ_r , and τ_f were observed. However, on the contrary, the photocurrent, R , and D^* experienced a negative effect (Figure 8b,c). For instance, when $n = 1$, that is 2D BA₂PbI₄, the dark current was measured as 6×10^{-13} A at 0.8 V, whilst under 200 μ W/cm² at a

1 V bias, the on/off ratio (current under light to dark current) was 10^4 , D^* was 1.6×10^{13} Jones, τ_r was 1.7 μ s, and τ_f was 3.9 μ s. For pure 2D materials, the controlled evaporation method was used to grow large-area ($>200 \text{ mm}^2$) 2D (PEA) $_2$ PbBr $_4$ single crystals (PEA $^+$: phenethylammonium, C $_8$ H $_9$ NH $_3^+$) [84]. Figure 8d shows the photo of the large 2D single crystal. The metal/crystal/metal device had an extremely low J_d of 10^{-13} A, large ON/OFF current ratio of 10^5 , D^* of 10^{13} Jones, and fast response speed of 0.4 ms. Figure 8e,f demonstrates the dark current noise at various frequencies and light intensity-dependent R and D^* data of the device fabricated with their 2D single crystals. Moreover, 2D perovskite material exhibited excellent stability over 3D perovskite. The single crystal in this work showed no degradation for up to four months under 45% of relative humidity. The comparison of 2D single-crystal and 3D single-crystal photodetectors reflects the effect of the quantum well structure. The insulating organic layers constrain the carriers in the inorganic layers. The carrier diffusion is greatly suppressed in both in-plane [85] and out-of-plane directions [86], leading to a low dark current, but also a low photocurrent. The long alkyl chains bring in additional resistances, consequently, low photoconduction and device performance. Still, 2D single crystals are highly promising for its high formation energy of defects and the suppression of ion migration. Chances lie in the effective use of the structure's advantages. More fundamental study is desired to pave the way for 2D single crystal applications.

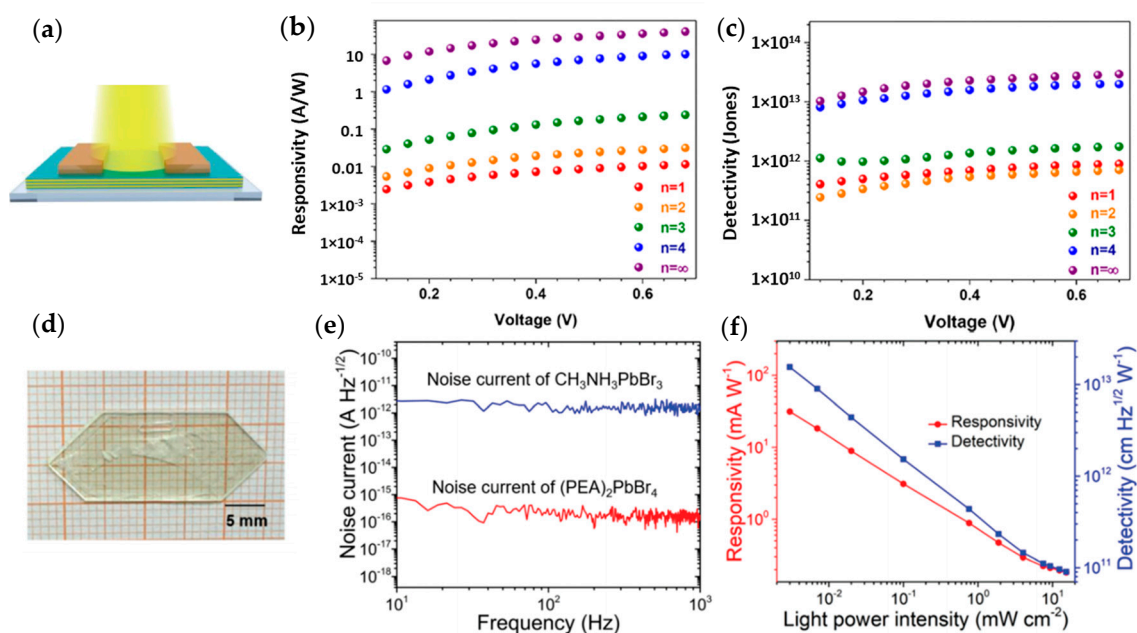


Figure 8. Schematic diagrams and performance of 2D perovskite single-crystal photodetectors. (a) Schematic diagram of the quasi-2D perovskite single crystal photodetector. Performance of photodetectors based on BA $_n$ MA $_{n-1}$ Pb $_n$ I $_{3n+1}$ quasi-2D perovskite single crystals with n of 1, 2, 3, 4, and ∞ including (b) responsivity, and (c) detectivity on bias voltages. Reproduced with permission from [36]. Copyright 2018, American Chemical Society. (d) Photograph of a transparent, $\sim 27 \times 11 \text{ mm}^2$ (PEA) $_2$ PbBr $_4$ single crystal. (e) Dark current noise at various frequencies of (PEA) $_2$ PbBr $_4$ and CH $_3$ NH $_3$ PbBr $_3$ single-crystal photodetectors at 10 V bias. (f) Light intensity-dependent R and D^* data of (PEA) $_2$ PbBr $_4$ photodetector at 10 V bias on light irradiance (365 nm). Reproduced from [84] with permission from The Royal Society of Chemistry, 2019.

4.3. Perovskite Single Crystals for X-ray Detectors

X-ray detectors absorb high-energy X-ray photons and convert them into charges. Briefly, the working mechanism involves two processes. One is the photoelectric effect process, where multiple carriers are generated by one X-ray photon due to its high energy. The other process is the Compton

scattering, where the incident photon passes energy to the electrons by scattering in the specific angle. The carriers are collected by electrodes, producing a signal current for further analysis. Conventional Si or Ge semiconductor-based or scintillator-based (such as NaI) X-ray detectors have the disadvantages of low energy resolution, high cost, and narrow operating temperature range. The newly developed materials such as CdZnTe, HgI, and TlBr still cannot meet the requirements of both low price and high detection efficiency and energy resolution, while perovskite single crystals provide opportunities for high sensitivity, high resolution radiation detectors.

The key operation factors for X-ray detectors are the X-ray attenuation coefficient, $\mu\tau$ product (where μ is the carrier mobility and τ is the carrier lifetime), sensitivity, detection limit, EQE, and responsivity R . Attenuation coefficient is the fraction of the intensity of the incident beam that is scattered and absorbed by per unit distance of the material. The strong penetration capability of X-ray requires a thicker semiconductor for charge generation. High attenuation coefficient benefits sufficient photon absorption with a small thickness, so the carriers will be generated across the semiconductor and be easily collected. The attenuated photons will be exported as the signal current [87]. At the same time, a lower dose of X-ray is required for detection using high-attenuation materials, ensuring a safer operating environment for technicians. The attenuation coefficient is proportional to Z^4/E^3 , where Z is the atomic number of the material and E is the energy of the X-ray photon. Figure 9a illustrates the thickness-dependent attenuation efficiency of different materials [88]. From the figure, the 2 mm-thick MAPbBr₃ crystal is enough to attenuate almost 100% of the X-ray due to the heavy Pb (Z of 82). The 2D perovskite material (NH₄)₂Bi₂I₉ exhibits higher attenuation with heavy Bi ($Z = 83$) and I ($Z = 53$). The $\mu\tau$ product is the average diffusion and drift distance under per unit of the electric field, it also means that under a given electric field, the charge collection efficiency will be higher, which can be calculated from the Hecht equation

$$I = \frac{I_0 \mu \tau V}{L^2} \frac{1 - \exp\left(-\frac{L^2}{\mu \tau V}\right)}{1 + \frac{L}{V} \frac{s}{\mu}} \quad (1)$$

where I is the photocurrent; I_0 is the saturated photocurrent; L is the thickness of the material thickness; V is the bias voltage; and s is the surface recombination velocity. As mentioned, the perovskite single crystal has excellent carrier dynamics of large carrier mobility μ and long carrier lifetime τ as a semiconductor, enabling sufficient charge collection and a larger $\mu\tau$ product.

As X-rays are high energy radiation, strict regulations are applied to the effective dose and accelerating potential, especially for medical use like computed tomography (CT). The X-ray beam aims at the human body and is attenuated to different degrees. The penetrated photons are detected and reveal localised information. As the radiation exposure is of high risk of developing cancer, the dose for each CT scan should be as low as possible. The detection limit explains the minimum dose rate for detection, meanwhile, sensitivity decides the resolution of the resultant image. The two work together to realize a high-quality image. Wei and coworkers first reported a highly sensitive X-ray detector made of MAPbBr₃ single crystals [17]. They passivated the crystal surface by UV-O₃ treatment for 20 min to oxidize the surface defects by hydroxyl bonds between the hydrogen and lead atoms. The passivated perovskite showed a longer radiative recombination lifetime, reduced trap density, and high $\mu\tau$ product of $1.2 \times 10^{-2} \text{ cm}^2 \text{V}^{-1}$. The X-ray device based on a 2 mm-thick MAPbBr₃ single crystal had a sensitivity of $80 \mu\text{C Gy}_{\text{air}}^{-1} \text{cm}^{-2}$ and a detection limit of $0.5 \mu\text{Gy}_{\text{air}} \text{s}^{-1}$. Later in 2017, they overcame the limitations of device noise and charge collection by alloying p-type doped MAPbBr₃ and n-type doped MAPbCl₃ into MAPbBr_{2.94}Cl_{0.06} [89]. Figure 9b compares the dark current density of MAPbBr₃, MAPbBr_{2.94}Cl_{0.06}, and MAPbBr_{2.85}Cl_{0.15} single-crystal devices with a thickness of $\sim 2 \text{ mm}$, where MAPbBr_{2.94}Cl_{0.06} exhibited the lowest dark in the $10^{-5} \text{ mA cm}^{-2}$ level with a high signal-to-noise ratio (Figure 9c). This alloyed MAPbBr_{2.94}Cl_{0.06} material exhibited threefold improved mobility of $560 \text{ cm}^2 \text{V}^{-1} \text{s}^{-1}$ than the pure MAPbBr₃, and $\mu\tau$ product of $1.8 \times 10^{-2} \text{ cm}^2 \text{V}^{-1}$. The resultant X-ray detector with the structure of Cr/MAPbBr_{3-x}Cl_x/C60/bathocuproine (BCP)/Cr had a

high sensitivity of $8.4 \times 10^4 \mu\text{C Gy}_{\text{air}}^{-1}\text{cm}^{-2}$, which is about 4000-fold higher than that of commercial α -Se X-ray detectors, with a detection limit of $7.6 \text{ nGy}_{\text{air}}\text{s}^{-1}$. The dose rate-dependent current density is shown in Figure 9d. Zhuang et al. reported an innovative 2D layered perovskite single crystal, $(\text{NH}_4)_3\text{Bi}_2\text{I}_9$, with a high $\mu\tau$ product of $1.1 \times 10^{-2} \text{ cm}^2\text{V}^{-1}$ [88]. Due to the suppressed carrier diffusion, 2D perovskite is always inferior to 3D for the $\mu\tau$ product, where it is interesting for $(\text{NH}_4)_3\text{Bi}_2\text{I}_9$ to have such high mobility. As they explained, the absence of the $\text{Bi}_2\text{I}_9^{3-}$ cluster dimer in the $(\text{NH}_4)_3\text{Bi}_2\text{I}_9$ structure is beneficial to delocalize the electron band, implying potentially better carrier mobility [90]. Unsurprisingly, the X-ray detector exhibited a sensitivity of $0.8 \times 10^4 \mu\text{C Gy}_{\text{air}}^{-1}\text{cm}^{-2}$, a detection limit of $210 \text{ nGy}_{\text{air}}\text{s}^{-1}$ much lower than the upper limit for medical diagnosis ($5.5 \mu\text{Gy}_{\text{air}}\text{s}^{-1}$).

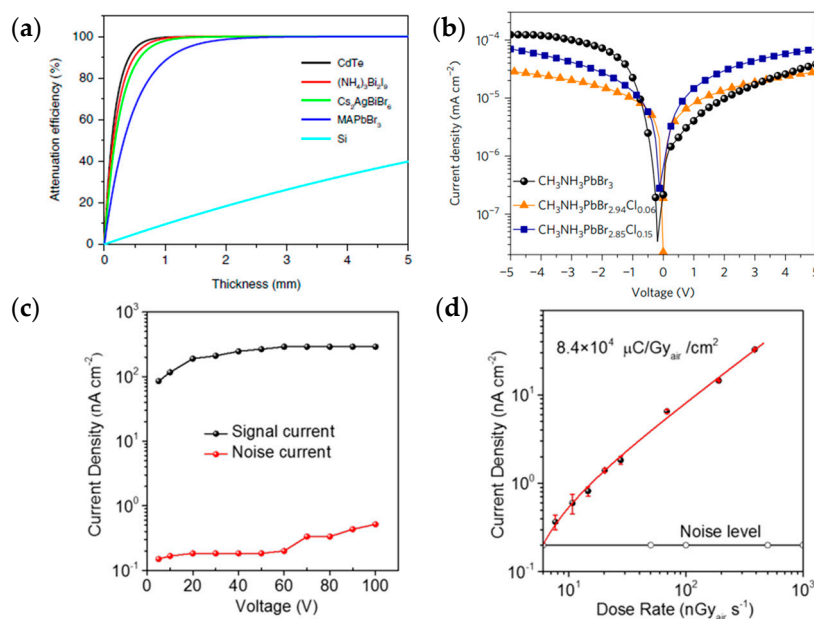


Figure 9. The performance of perovskite single-crystal X-ray detectors. (a) Attenuation efficiencies of $(\text{NH}_4)_3\text{Bi}_2\text{I}_9$, $\text{Cs}_2\text{AgBiBr}_6$, MAPbBr_3 , CdTe , and Si semiconductors to 50 keV X-ray photons versus thickness. Reproduced with permission from [88]. Copyright 2019, Springer Nature. (b) Dark current density of MAPbBr_3 , $\text{MAPbBr}_{2.94}\text{Cl}_{0.06}$, and $\text{MAPbBr}_{2.85}\text{Cl}_{0.15}$ single-crystal devices with thickness of $\sim 2 \text{ mm}$. (c) Current density output to 8 keV X-rays with a dose rate of $2.4 \mu\text{Gy}_{\text{air}}\text{s}^{-1}$ and noise current density of a 1 mm thick $\text{MAPbBr}_{2.94}\text{Cl}_{0.06}$ single crystal device as applied voltage. (d) Dose rate-dependent current density output of 1 mm thick $\text{MAPbBr}_{2.94}\text{Cl}_{0.06}$ single crystal device to 8 keV X-rays. A sensitivity of $8.4 \times 10^4 \mu\text{C Gy}_{\text{air}}^{-1}\text{cm}^{-2}$ was derived from the slope of the fitting line. Reproduced with permission from [89]. Copyright 2017, Springer Nature.

5. Strategic Approaches for Advancing Perovskite Single Crystal-Based Applications and Recommendations

There is no doubt that perovskite single crystals featuring superior optical properties are promising for photovoltaics. However, with regard to device performance, the single crystal drops behind the polycrystalline thin film counterpart, even though it holds advanced crystallinity. Herein, several innovative approaches and optimisation strategies are summarised, followed by the existing challenges.

5.1. Synthesis Process

Defects are interruptions of regular patterns in crystals due to the misplacement of atoms and lattice mismatching. All defects create electron transition levels in the forbidden region. Deep-level traps are located near the centre of the forbidden gap, which can work as the recombination centres that trap carriers, resulting in non-radiative recombination. Non-radiative recombination is fatal for the performance of photovoltaic applications as the trapped carriers are lost, cannot reach and be collected

by electrodes, and generate an external current. High-quality single crystals exhibit a several orders of magnitudes lower (10^9 – 10^{11} cm $^{-3}$) defect density than that of thin films (10^{16} – 10^{18} cm $^{-3}$), which is dominated by the synthesis process. However, the conventional crystallisation methods of AVC, STL, and ITC are adapted from methods for other materials, so an optimisation of the process is called for.

A stable environment is critical for crystallisation. The factors include temperature, vibration, humidity, etc. The supersaturation state, a metastable state of the solution, would collapse due to sudden disturbance, resulting in massive nucleation and lattice distortion. The low-temperature-gradient crystallisation (LTGC) method aims at eliminating the negative influence of the quick temperature change in the conventional ITC method [91]. When heating up the solution to induce supersaturation, the heating rate was as low as 2 °C per day. A $44 \times 49 \times 17$ mm large MAPbBr $_3$ single crystal was harvested after 18 days, which displayed a carrier mobility of 81 ± 5 cm 2 V $^{-1}$ s $^{-1}$, a carrier lifetime of 899 ± 127 ns, and a trap density of $6.2 \pm 2.7 \times 10^9$ cm $^{-3}$. Its application of a photodetector had a detectivity of 6×10^{13} Jones and response speed of 40 μ s. The large area also enabled integrated projection imaging, consisting of a sensor array of 729 pixels (Figure 10a–c). Though the low heating rate minimised the massive nucleation, the thermal gradient still generated convective currents that would disturb the ordered crystal growth and induce defects. Crystallisation at room temperature is developed as a solution to the heat-induced structure distortion. One of the methods is room-temperature liquid diffused separation induced crystallisation, as reported by Yao et al. [92]. A certain amount of silicone oil was added in the precursor as a separation medium. With the diffusion of the solvent into silicone oil, the concentration of the precursor gradually decreased and reached supersaturation for crystallisation. The process is illustrated in Figure 10d. The trap density of as-grown MAPbBr $_3$ single crystal was lower (4.4×10^9 cm $^{-3}$) than the trap density of crystals grown at 90 °C (2.2×10^{10} cm $^{-3}$). However, it took several days to obtain a 4-mm sized MAPbBr $_3$ crystal compared with several hours by the conventional high temperature ITC method. Basically, synthesis methods are developing toward a low-temperature and low-rate. It should be considered whether the enhancement on quality is worth sacrificing the growth efficiency.

Crystallisation of one crystal is usually repeated several times in fresh precursor to obtain the desired size. It inevitably causes defects and lattice mismatching when transferring into a new solution environment. The seed dissolution-regrowth (SDR) method overcomes the structural inconsistency between the nucleus and the surface of the seed crystal by keeping the precursor at a relatively low temperature after seeding and prior to heating to the target growth temperature [81]. This allows for the existing impurities on the seed surface to dissolve back and improve the structural matching. SEM images confirmed the dense and uniform structure of the SDR-crystals compared with the loose inner structure of the conventional-ITC-grown crystals, as shown in Figure 10e,f. Another strategy overcomes the mismatching between the nuclei and seed surface by removing low quality seeds. The nucleation-controlled growth method refines the precursor solution by the pre-growth of seeds to reduce nucleation sites [93]. The precursor is heated at high temperature for massive nucleation, which is then filtered and used for crystal growth with high-quality seeds. This refining step ensures the independent growth of each nuclei and removes impurities that form irregular seeds. The as-grown Cs $_3$ Bi $_2$ I $_9$ crystal was made into an X-ray detector that exhibited a high sensitivity of 1652.3 μ C Gy $_{\text{air}}^{-1}$ cm $^{-2}$ and very low detection limit of 130 nGy $_{\text{air}}$ s $^{-1}$.

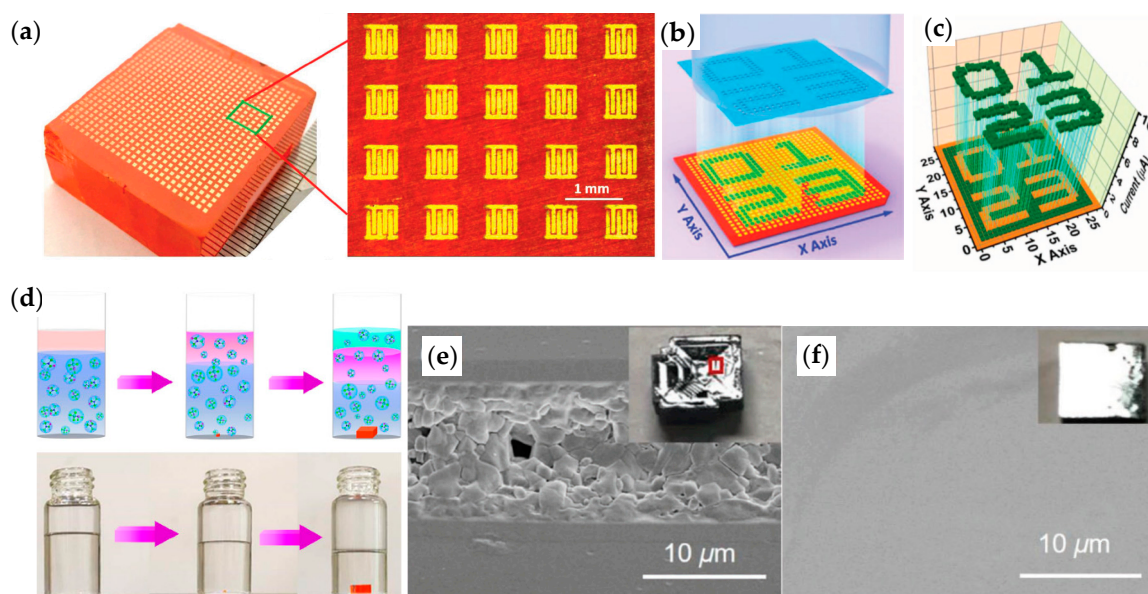


Figure 10. Images and illustrations of perovskite single crystals grown by modified synthesis method, and applications. (a) Photographs of a photosensor array of 729 pixels, fabricated on a large MAPbBr₃ single crystal; (b) schematic diagram of the projection imaging mechanism; and (c) the corresponding photocurrent outputs from each pixel measured at 2 V bias with an optical pattern of “0123”. A patterned mask was placed directly above the imaging assembly. Under light illumination, the patterned mask is projected through the mask with bright and shadow contrast to form the image of the mask on the sensor unit. Reproduced with permission from [91]. Copyright 2018, WILEY-VCH. (d) Schematic diagram of the room-temperature liquid diffused separation induced crystallisation method. Reproduced with permission from [92]. Copyright 2020, Springer Nature. (e,f) SEM images of cuboid MAPbI₃ single crystals synthesised by typical ITC and SDR. The insets are the photographs of the crystals, for which SEM images taken. Reproduced with permission from [81]. Copyright 2018, WILEY-VCH.

5.2. Surface Modifications

For single crystals, the surface is critical. Due to the absence of grain boundaries in the bulk, the surfaces have a much higher concentration of defects than the bulk, which will give rise to severe recombination. Moreover, the surface recombination velocity of single crystals ($2.8 \times 10^3 \text{ cm s}^{-1}$) was reported to be nearly six times that of polycrystalline thin films ($0.45 \times 10^3 \text{ cm s}^{-1}$) [53]. X-ray photoelectron spectroscopy (XPS) results indicated a Pb-rich surface of single crystals, while polycrystalline thin films had a C- and N-rich surface. This is possibly due to the escape of MAI from the crystal lattice, resulted from the high crystallisation temperature [26] and partial dissolution by the residual solution on the surface [4]. Spin-coating MAI on the crystal surface for defect passivation was confirmed to be effective in enhancing the device efficiency [8]. Preserving and replenishing MAI on the surface are likely to complete surface structure and passivate vacancy defects. However, the understanding of the crystal surface is still lacking. For most of the reported trap density, the quantitative results only reflect the average trap density of the whole crystal. The low density of the interior of a single crystal drags down the overall level; the defective surface is easily overlooked. In addition to the lack of quantitative analysis, surface characterisations such as surface element distribution and surface recombination velocity are not well presented. Systematic study of the passivation effect is highly desired when designing new surface treatment strategies. For polycrystalline thin films, passivation of deep-level defects is realised through coordinate bonding, ionic bonding, and coordination of large band-gap material [94]. For example, depositing a 2D perovskite capping layer on top of the 3D perovskite thin film successfully improved V_{OC} , FF, PCE, and the stability of 3D perovskite thin film solar cells [12,95]. Single crystals can adopt the ideas from thin films and realize

overtaking. One problem is that the conventional method of spin-coating the passivation layer may lead to dissolution of the crystal surface, consequently inducing more defects. Caution should be paid when choosing the solvent.

Degradation is one of the serious weaknesses of perovskite. Single crystals are much more stable than polycrystalline thin films. Even so, single crystals experience fast decomposition and degradation of the surface. After a long period of exposure in oxygen and moisture, the crystal surfaces of MAPbBr₃ are prone to form a hydrate and polycrystalline surface [96], as shown in Figure 11a–c. Aged surfaces showed differences in band gap, PL position, light absorbance, and carrier lifetime with a pristine fresh surface, which were similar to those of polycrystalline thin films. This study lays stress that the preservation of the single-crystalline surface from degradation is as vital as the treatment afterward.

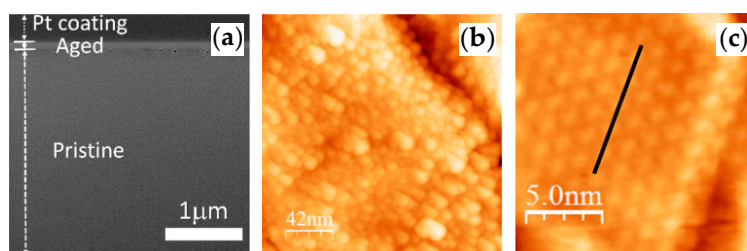


Figure 11. Real-space imaging and visualization of MAPbBr₃ single crystals. (a) Cross-sectional Focused Ion Beam Scanning Electron Microscopy (FIB-SEM) image showing clear contrast differences on the aged and pristine surfaces; Scanning Tunnelling Microscopy (STM) images of a MAPbBr₃ crystal obtained from the (b) aged surface and (c) pristine surface showing the ordered structures with well-aligned stacked planes. Reproduced with permission from [96]. Copyright 2016, American Chemical Society. Further permissions related to the material excerpted should be directed to the ACS.

5.3. Interface Engineering

Layer-structure optoelectronic devices require intimate contact between each layer, in order to confirm efficient carrier transport and reduce ohmic loss as well as facilitating fabrication. Attaching freestanding perovskite single crystals on functional substrates is challenging due to the weak interactions of hydrogen bonds and van der Waals forces between them. Commonly, the space-confined solution-process method is viable for the direct growth of crystals on substrates, but Newton's rings and voids exist between the thin crystal and the substrate, even for the champion device [26,78]. Phase transition is likely to be the origin. Huang's group seeded perovskite on modified Si wafer, which was treated by brominated (3-aminopropyl) triethoxysilane (APTES) [97]. The interlayer with functional groups strengthens the interaction. The hydrolysis of Si–O–C₂H₅ groups form strong covalent Si–O–Si bonds with the –OH on the Si, and the [–Si(CH₂)₃NH₃]⁺ binds to the [PbBr₃][−] octahedra of MAPbBr₃ perovskite, as illustrated in Figure 12a. The interaction overcame a pulling force of 10 g. Their X-ray detection device with the Au/BCP/C₆₀/MAPbBr₃/Si structure had a sensitivity of $2.1 \times 10^4 \mu\text{C Gy}_{\text{air}}^{-1} \text{cm}^{-2}$ under 8 keV X-ray radiation. Still, the interlayer induced extra defects at the interfaces. Recently, without the interlay, MAPbBr₃ was directly grown on the Si wafer with an improved interface, the interaction of which overcame a pulling force of 50 g [98]. Rather than grown by the ITC method, AVC was chosen for better control of the crystallisation rate. Si wafer was put in the precursor as demonstrated in Figure 12b. The similar lattice constants of Si and MAPbBr₃ are beneficial for epitaxial growth. The resultant Si/perovskite/Au photodetector had a broad detection range from 405 nm to 1064 nm, a detectivity of 5.9×10^{10} Jones, and ultrafast response time of τ_r 520 ns, ascribing to intimate contact. Adding the interlayer and finding suitable substrates with similar lattice constants are two directions to optimize the contact between single crystals and conductive substrates, which should work together with thin film fabrication. However, one of the challenges is how to attain good contact while maintaining sufficient ion diffusion for single-crystalline thin film growth in the narrow gap between two substrates.

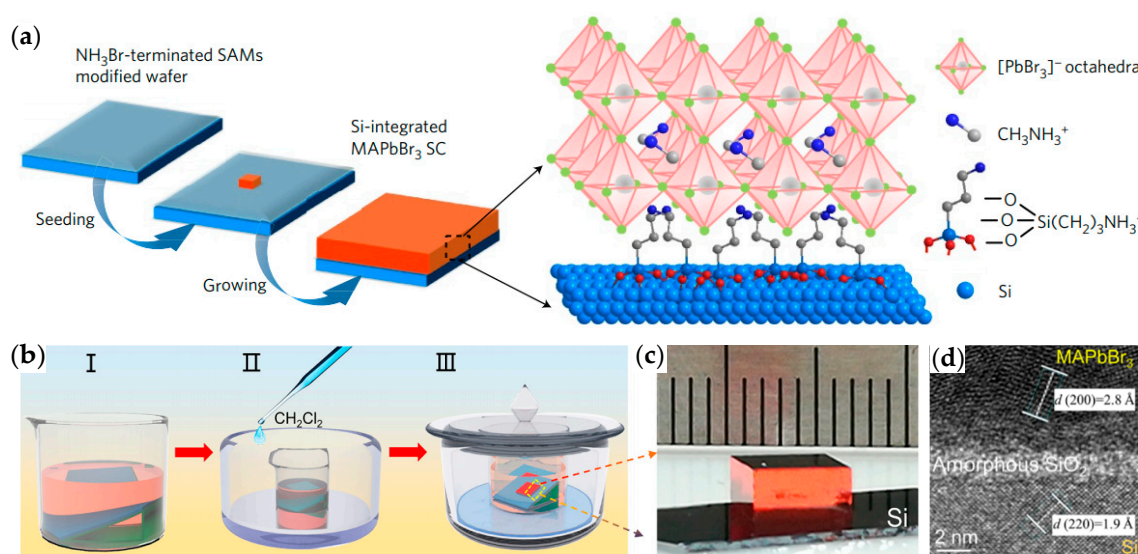


Figure 12. Schematic diagrams and images of interface engineering between perovskite single crystal and functional substrates. (a) Schematic diagrams of three steps of the fabrication of Si-integrated MAPbBr₃ single crystals (not to scale, the silane thickness is highly exaggerated for clarity): I, modified Si wafer was placed in MAPbBr₃ precursor solution; II, the small beaker was placed in a weighing bottle with CH₂Cl₂; III, the bottle was sealed and the saturated antisolvent (CH₂Cl₂) vapor inside slowly diffuses into the precursor solution, leading to the precipitation of MAPbBr₃ single crystals on the modified Si substrate. Reproduced with permission from [97]. Copyright 2017, Springer Nature. (b) Schematic diagram of the optimised antisolvent vapor-assisted crystallisation method for integrating single crystal MAPbBr₃ on the Si substrate; (c) photograph of the Si-integrated MAPbBr₃ single crystal, and (d) cross-sectional high-resolution Transmission Electron Microscopy (TEM) image of the interface between the Si and MAPbBr₃ crystal. Reproduced with permission from [98]. Copyright 2020, American Chemical Society.

5.4. Regulation of Dimensions

Practical applications of single crystals desire a large area of more than several tens of square millimetres and thickness below tens of micrometres. How to obtain the desired dimensions, while still keeping high crystallinity is one of the biggest challenges for single crystals. For state-of-art single-crystal solar cells, the thickness of the perovskite layer is hardly below 10 µm. It is speculated that inefficient ion diffusion into the narrow space between substrates during the crystallisation would be the main reason for the formation of the cracks and the low crystallinity. Though theoretical calculation revealed high PCE can be obtained when the crystal thickness is around 200 µm [8], thin crystals from space-confined crystallisation are not comparable with freestanding crystals with regard to optoelectrical properties, especially for carrier diffusion length. The key point is to balance the growth rate and nucleation rate. The former determines the growth efficiency. The later should be minimised to ensure fewer nuclei sites and avoid lattice distortion caused by the combination of other nuclei. On the other hand, high-quality thin crystals from the top-down method have damaged crystal surfaces, which triggers new challenges of surface treatment and substrate incompatibility. Systematic surface characterisation gives support to designing rational slicing strategies and surface modifications.

6. Summary

In summary, perovskite single crystals stand out as one of the most promising semiconductor materials to be applied in optoelectronic applications. Various synthesis methods have been developed, aiming at harvesting high-quality and large-size single crystals. The as-obtained single crystals showed excellent performance in the fields of photodetectors and X-ray detectors, even better than commercialised semiconductor counterparts such as α-Se. As required by the device fabrication,

controlling the thickness of single crystals down to at least the μm -scale is one of the prerequisites for high-performance applications, especially for solar cells. Device performance can be further boosted with smaller crystal thickness. Adapted from conventional crystallisation methods, advanced fabrication strategies have successfully realised confinement on the thickness of single crystal thin film from hundreds of nm to tens of μm . The champion single-crystal solar cell has a PCE of 21.93%, but still there is a huge gap between the single-crystal device and polycrystalline perovskite thin film counterpart (25.2%). Major obstacles for the development of perovskite single crystal applications are the surface defects and compatibility with functional layers. Fundamental study and quantitative analysis for the exploration of single crystal surface defect type and properties are lacking. In addition, single crystal thin films experience different surface states with bulk single crystals, arising from the influence of substrates and the slicing process. Therefore, systematic characterisation of surface defects is needed to point out the direction for surface treatment. Effective solutions could be learned from the experience of surface passivation strategies for polycrystalline thin films. On the other hand, the contact between the single crystal and the functional layer is not perfect. The voids could hinder carrier transportation and thus affect the device performance. Adding interlayers is viable to strengthen interactions, but the additional defects at the interfaces should be seriously considered. Efforts need to be focused on modifying the crystallisation process toward low-temperature and steady processing in order to minimise structure disorder. For practical applications, large area and controlled thickness are essential. The study on the crystallisation mechanism and defect engineering should run in parallel. It is expected that perovskite single crystals will soon surpass their polycrystalline counterpart and become an excellent alternative for optoelectronic applications.

Author Contributions: Y.Z. wrote the original draft of the paper under supervision of J.-H.Y. and L.W. M.L., J.-H.Y., and L.W. conceptualised and designed the structure of the work. M.L., T.Q., E.H., I.K.K., M.-C.J. Y.H.N. L.W., and J.-H.Y. revised the paper. All authors have read and agreed to the published version of the manuscript.

Funding: This research received no external funding.

Acknowledgments: This research has been financially supported by the Australian Research Council (ARC) through its Discovery and DECRA programs, and also supported by funding from the Faculty of Pure and Applied Sciences in University of Tsukuba (Japan).

Conflicts of Interest: The authors declare no conflict of interest.

References

1. Weber, D. $\text{CH}_3\text{NH}_3\text{SnBr}_x\text{I}_{3-x}$ ($x = 0-3$)—Sn(II)-system with cubic perovskite structure. *Z. Fur Nat. Sect. B J. Chem. Sci.* **1978**, *33*, 862–865.
2. Weber, D. $\text{CH}_3\text{NH}_3\text{PbX}_3$, a Pb(II)-system with cubic perovskite structure. *Z. Fur Nat. Sect. B J. Chem. Sci.* **1978**, *33*, 1443–1445.
3. Kojima, A.; Teshima, K.; Shirai, Y.; Miyasaka, T. Organometal halide perovskites as visible-light sensitizers for photovoltaic cells. *J. Am. Chem. Soc.* **2009**, *131*, 6050–6051. [[CrossRef](#)]
4. Dong, Q.; Fang, Y.; Shao, Y.; Mulligan, P.; Qiu, J.; Cao, L.; Huang, J. Electron-Hole diffusion lengths $> 175\ \mu\text{m}$ in solution-grown $\text{CH}_3\text{NH}_3\text{PbI}_3$ single crystals. *Science* **2015**, *347*, 967–970. [[CrossRef](#)] [[PubMed](#)]
5. Shi, D.; Adinolfi, V.; Comin, R.; Yuan, M.; Alarousu, E.; Buin, A.; Chen, Y.; Hoogland, S.; Rothenberger, A.; Katsiev, K.; et al. Low trap-state density and long carrier diffusion in organolead trihalide perovskite single crystals. *Science* **2015**, *347*, 519–522. [[CrossRef](#)] [[PubMed](#)]
6. Wehrenfennig, C.; Eperon, G.E.; Johnston, M.B.; Snaith, H.J.; Herz, L.M. High charge carrier mobilities and lifetimes in organolead trihalide perovskites. *Adv. Mater.* **2014**, *26*, 1584–1589. [[CrossRef](#)]
7. Lim, J.; Hörantner, M.T.; Sakai, N.; Ball, J.M.; Mahesh, S.; Noel, N.K.; Lin, Y.H.; Patel, J.B.; McMeekin, D.P.; Johnston, M.B.; et al. Elucidating the long-range charge carrier mobility in metal halide perovskite thin films. *Energy Environ. Sci.* **2019**, *12*, 169–176. [[CrossRef](#)]
8. Chen, Z.; Dong, Q.; Liu, Y.; Bao, C.; Fang, Y.; Lin, Y.; Tang, S.; Wang, Q.; Xiao, X.; Bai, Y.; et al. Thin single crystal perovskite solar cells to harvest below-bandgap light absorption. *Nat. Commun.* **2017**, *8*, 1890. [[CrossRef](#)]

9. Amat, A.; Mosconi, E.; Ronca, E.; Quarti, C.; Umari, P.; Nazeeruddin, M.K.; Gratzel, M.; De Angelis, F. Cation-Induced band-gap tuning in organohalide perovskites: Interplay of spin–orbit coupling and octahedra tilting. *Nano Lett.* **2014**, *14*, 3608–3616. [\[CrossRef\]](#)
10. National Renewable Energy Laboratory. Best Research-Cell Efficiency Chart. Available online: <https://www.nrel.gov/pv/cell-efficiency.html> (accessed on 9 March 2020).
11. Park, N.-G. Perovskite solar cells: An emerging photovoltaic technology. *Mater. Today* **2015**, *18*, 65–72. [\[CrossRef\]](#)
12. Hu, Y.; Schlipf, J.; Wussler, M.; Petrus, M.L.; Jaegermann, W.; Bein, T.; Müller-Buschbaum, P.; Docampo, P. Hybrid perovskite/perovskite heterojunction solar cells. *ACS Nano* **2016**, *10*, 5999–6007. [\[CrossRef\]](#) [\[PubMed\]](#)
13. Yoo, E.J.; Lyu, M.; Yun, J.H.; Kang, C.J.; Choi, Y.J.; Wang, L. Resistive switching behavior in organic–inorganic hybrid $\text{CH}_3\text{NH}_3\text{PbI}_{3-x}\text{Cl}_x$ perovskite for resistive random access memory devices. *Adv. Mater.* **2015**, *27*, 6170–6175. [\[CrossRef\]](#) [\[PubMed\]](#)
14. Gu, C.; Lee, J.-S. Flexible hybrid organic–inorganic perovskite memory. *ACS Nano* **2016**, *10*, 5413–5418. [\[CrossRef\]](#) [\[PubMed\]](#)
15. Fang, Y.; Dong, Q.; Shao, Y.; Yuan, Y.; Huang, J. Highly narrowband perovskite single-crystal photodetectors enabled by surface-charge recombination. *Nat. Photonics* **2015**, *9*, 679. [\[CrossRef\]](#)
16. Leung, S.F.; Ho, K.T.; Kung, P.K.; Hsiao, V.K.; Alshareef, H.N.; Wang, Z.L.; He, J.H. A self-powered and flexible organometallic halide perovskite photodetector with very high detectivity. *Adv. Mater.* **2018**, *30*, 1704611. [\[CrossRef\]](#)
17. Wei, H.; Fang, Y.; Mulligan, P.; Chuirazzi, W.; Fang, H.H.; Wang, C.; Ecker, B.R.; Gao, Y.; Loi, M.A.; Cao, L.; et al. Sensitive X-ray detectors made of methylammonium lead tribromide perovskite single crystals. *Nat. Photonics* **2016**, *10*, 333. [\[CrossRef\]](#)
18. Yakunin, S.; Sytnyk, M.; Kriegner, D.; Shrestha, S.; Richter, M.; Matt, G.J.; Azimi, H.; Brabec, C.J.; Stangl, J.; Kovalenko, M.V.; et al. Detection of X-ray photons by solution-processed lead halide perovskites. *Nat. Photonics* **2015**, *9*, 444–449. [\[CrossRef\]](#)
19. Lin, K.; Xing, J.; Quan, L.N.; de Arquer, F.P.G.; Gong, X.; Lu, J.; Xie, L.; Zhao, W.; Zhang, D.; Yan, C.; et al. Perovskite light-emitting diodes with external quantum efficiency exceeding 20 per cent. *Nature* **2018**, *562*, 245–248. [\[CrossRef\]](#)
20. Wang, N.; Cheng, L.; Ge, R.; Zhang, S.; Miao, Y.; Zou, W.; Yi, C.; Sun, Y.; Cao, Y.; Yang, R.; et al. Perovskite light-emitting diodes based on solution-processed self-organized multiple quantum wells. *Nat. Photonics* **2016**, *10*, 699–704. [\[CrossRef\]](#)
21. Wenger, B.; Nayak, P.K.; Wen, X.; Kesava, S.V.; Noel, N.K.; Snaith, H.J. Consolidation of the optoelectronic properties of $\text{CH}_3\text{NH}_3\text{PbBr}_3$ perovskite single crystals. *Nat. Commun.* **2017**, *8*, 590. [\[CrossRef\]](#)
22. Zhang, Y.; Liu, Y.; Yang, Z.; Liu, S.F. High-Quality perovskite MAPbI_3 single crystals for broad-spectrum and rapid response integrate photodetector. *J. Energy Chem.* **2018**, *27*, 722–727. [\[CrossRef\]](#)
23. Saidaminov, M.I.; Abdelhady, A.L.; Murali, B.; Alarousu, E.; Burlakov, V.M.; Peng, W.; Dursun, I.; Wang, L.; He, Y.; Maculan, G.; et al. High-Quality bulk hybrid perovskite single crystals within minutes by inverse temperature crystallization. *Nat. Commun.* **2015**, *6*, 1–6. [\[CrossRef\]](#) [\[PubMed\]](#)
24. Yang, Y.; Yan, Y.; Yang, M.; Choi, S.; Zhu, K.; Luther, J.M.; Beard, M.C. Low surface recombination velocity in solution-grown $\text{CH}_3\text{NH}_3\text{PbBr}_3$ perovskite single crystal. *Nat. Commun.* **2015**, *6*, 7961. [\[CrossRef\]](#) [\[PubMed\]](#)
25. Steele, J.A.; Pan, W.; Martin, C.; Keshavarz, M.; Debroye, E.; Yuan, H.; Banerjee, S.; Fron, E.; Jonckheere, D.; Kim, C.W.; et al. Photophysical pathways in highly sensitive $\text{Cs}_2\text{AgBiBr}_6$ double-perovskite single-crystal X-ray detectors. *Adv. Mater.* **2018**, *30*, 1804450. [\[CrossRef\]](#) [\[PubMed\]](#)
26. Alsalloum, A.Y.; Turedi, B.; Zheng, X.; Mitra, S.; Zhumekenov, A.A.; Lee, K.J.; Maity, P.; Gereige, I.; AlSaggaf, A.; Roqan, I.S.; et al. Low temperature crystallization enables 21.9% efficient single-crystal MAPbI_3 inverted perovskite solar cells. *ACS Energy Lett.* **2020**, *5*, 657–662. [\[CrossRef\]](#)
27. Chen, Y.X.; Ge, Q.Q.; Shi, Y.; Liu, J.; Xue, D.J.; Ma, J.Y.; Ding, J.; Yan, H.J.; Hu, J.S.; Wan, L.J. General space-confined on-substrate fabrication of thickness-adjustable hybrid perovskite single-crystalline thin films. *J. Am. Chem. Soc.* **2016**, *138*, 16196–16199. [\[CrossRef\]](#)
28. Yang, Z.; Deng, Y.; Zhang, X.; Wang, S.; Chen, H.; Yang, S.; Khurgin, J.; Fang, N.X.; Zhang, X.; Ma, R. High-Performance single-crystalline perovskite thin-film photodetector. *Adv. Mater.* **2018**, *30*, 1704333. [\[CrossRef\]](#)

29. Lee, L.; Baek, J.; Park, K.S.; Lee, Y.-E.; Shrestha, N.K.; Sung, M.M. Wafer-Scale single-crystal perovskite patterned thin films based on geometrically-confined lateral crystal growth. *Nat. Commun.* **2017**, *8*, 1–8. [[CrossRef](#)]
30. Song, Y.; Bi, W.; Wang, A.; Liu, X.; Kang, Y.; Dong, Q. Efficient lateral-structure perovskite single crystal solar cells with high operational stability. *Nat. Commun.* **2020**, *11*, 1–8. [[CrossRef](#)]
31. Sung, H.-H.; Kuo, C.-C.; Chiang, H.-S.; Yue, H.-L.; Chen, F.-C. Differential space-limited crystallization of mixed-cation lead iodide single-crystal micro-plates enhances the performance of perovskite solar cells. *Solar RRL* **2019**, *3*, 1900130. [[CrossRef](#)]
32. Liu, Y.; Yang, Z.; Liu, S. Recent progress in single-crystalline perovskite research including crystal preparation, property evaluation, and applications. *Adv. Sci.* **2018**, *5*, 1700471. [[CrossRef](#)] [[PubMed](#)]
33. Jacobsson, T.J.; Pazoki, M.; Hagfeldt, A.; Edvinsson, T. Goldschmidt's rules and strontium replacement in lead halogen perovskite solar cells: Theory and preliminary experiments on $\text{CH}_3\text{NH}_3\text{SrI}_3$. *J. Phys. Chem. C* **2015**, *119*, 25673–25683. [[CrossRef](#)]
34. Eames, C.; Frost, J.M.; Barnes, P.R.; O'regan, B.C.; Walsh, A.; Islam, M.S. Ionic transport in hybrid lead iodide perovskite solar cells. *Nat. Commun.* **2015**, *6*, 1–8. [[CrossRef](#)] [[PubMed](#)]
35. Yang, Z.; Chueh, C.C.; Liang, P.W.; Crump, M.; Lin, F.; Zhu, Z.; Jen, A.K.Y. Effects of formamidinium and bromide ion substitution in methylammonium lead triiodide toward high-performance perovskite solar cells. *Nano Energy* **2016**, *22*, 328–337. [[CrossRef](#)]
36. Wang, K.; Wu, C.; Yang, D.; Jiang, Y.; Priya, S. Quasi-Two-Dimensional halide perovskite single crystal photodetector. *ACS Nano* **2018**, *12*, 4919–4929. [[CrossRef](#)] [[PubMed](#)]
37. Stoumpos, C.C.; Cao, D.H.; Clark, D.J.; Young, J.; Rondinelli, J.M.; Jang, J.I.; Hupp, J.T.; Kanatzidis, M.G. Ruddlesden–Popper hybrid lead iodide perovskite 2D homologous semiconductors. *Chem. Mater.* **2016**, *28*, 2852–2867. [[CrossRef](#)]
38. Eperon, G.E.; Stranks, S.D.; Menelaou, C.; Johnston, M.B.; Herz, L.M.; Snaith, H.J. Formamidinium lead trihalide: A broadly tunable perovskite for efficient planar heterojunction solar cells. *Energy Environ. Sci.* **2014**, *7*, 982–988. [[CrossRef](#)]
39. Zhao, Y.; Zhu, K. Efficient planar perovskite solar cells based on 1.8 eV band gap $\text{CH}_3\text{NH}_3\text{PbI}_2\text{Br}$ nanosheets via thermal decomposition. *J. Am. Chem. Soc.* **2014**, *136*, 12241–12244. [[CrossRef](#)]
40. Yi, C.; Luo, J.; Meloni, S.; Boziki, A.; Ashari-Astani, N.; Grätzel, C.; Zakeeruddin, S.M.; Röthlisberger, U.; Grätzel, M. Entropic stabilization of mixed A-cation ABX_3 metal halide perovskites for high performance perovskite solar cells. *Energy Environ. Sci.* **2016**, *9*, 656–662. [[CrossRef](#)]
41. Noh, J.H.; Im, S.H.; Heo, J.H.; Mandal, T.N.; Seok, S.I. Chemical management for colorful, efficient, and stable inorganic–organic hybrid nanostructured solar cells. *Nano Lett.* **2013**, *13*, 1764–1769. [[CrossRef](#)]
42. Kim, D.; Yun, J.H.; Lyu, M.; Kim, J.; Lim, S.; Yun, J.S.; Wang, L.; Seidel, J. Probing facet dependent surface defects in MAPbI_3 perovskite single crystals. *J. Phys. Chem. C* **2019**, *123*, 14144–14151. [[CrossRef](#)]
43. Jao, M.-H.; Lu, C.-F.; Tai, P.-Y.; Su, W.-F. Precise facet engineering of perovskite single crystals by ligand-mediated strategy. *Cryst. Growth Des.* **2017**, *17*, 5945–5952. [[CrossRef](#)]
44. Chen, Q.; De Marco, N.; Yang, Y.M.; Song, T.B.; Chen, C.C.; Zhao, H.; Hong, Z.; Zhou, H.; Yang, Y. Under the spotlight: The organic–inorganic hybrid halide perovskite for optoelectronic applications. *Nano Today* **2015**, *10*, 355–396. [[CrossRef](#)]
45. de Quilletes, D.W.; Vorpahl, S.M.; Stranks, S.D.; Nagaoka, H.; Eperon, G.E.; Ziffer, M.E.; Snaith, H.J.; Ginger, D.S. Impact of microstructure on local carrier lifetime in perovskite solar cells. *Science* **2015**, *348*, 683–686. [[CrossRef](#)] [[PubMed](#)]
46. Yun, J.S.; Seidel, J.; Kim, J.; Soufiani, A.M.; Huang, S.; Lau, J.; Jeon, N.J.; Seok, S.I.; Green, M.A.; Ho-Baillie, A. Critical role of grain boundaries for ion migration in formamidinium and methylammonium lead halide perovskite solar cells. *Adv. Energy Mater.* **2016**, *6*, 1600330. [[CrossRef](#)]
47. Chen, Y.; He, M.; Peng, J.; Sun, Y.; Liang, Z. Structure and growth control of organic–inorganic halide perovskites for optoelectronics: From polycrystalline films to single crystals. *Adv. Sci.* **2016**, *3*, 1500392. [[CrossRef](#)] [[PubMed](#)]
48. Ran, C.; Xu, J.; Gao, W.; Huang, C.; Dou, S. Defects in metal triiodide perovskite materials towards high-performance solar cells: Origin, impact, characterization, and engineering. *Chem. Soc. Rev.* **2018**, *47*, 4581–4610. [[CrossRef](#)]

49. Horowitz, G. Validity of the concept of band edge in organic semiconductors. *J. Appl. Phys.* **2015**, *118*, 115502. [\[CrossRef\]](#)
50. Bi, Y.; Hutter, E.M.; Fang, Y.; Dong, Q.; Huang, J.; Savenije, T.J. Charge carrier lifetimes exceeding 15 μ s in methylammonium lead iodide single crystals. *J. Phys. Chem. Lett.* **2016**, *7*, 923–928. [\[CrossRef\]](#)
51. Zhang, F.; Yang, B.; Li, Y.; Deng, W.; He, R. Extra long electron-hole diffusion lengths in $\text{CH}_3\text{NH}_3\text{PbI}_{3-x}\text{Cl}_x$ perovskite single crystals. *J. Mater. Chem. C* **2017**, *5*, 8431–8435. [\[CrossRef\]](#)
52. Li, Y.; Yan, W.; Li, Y.; Wang, S.; Wang, W.; Bian, Z.; Xiao, L.; Gong, Q. Direct observation of long electron-hole diffusion distance in $\text{CH}_3\text{NH}_3\text{PbI}_3$ perovskite thin film. *Sci. Rep.* **2015**, *5*, 14485. [\[CrossRef\]](#) [\[PubMed\]](#)
53. Yang, Y.; Yang, M.; Moore, D.T.; Yan, Y.; Miller, E.M.; Zhu, K.; Beard, M.C. Top and bottom surfaces limit carrier lifetime in lead iodide perovskite films. *Nat. Energy* **2017**, *2*, 1–7. [\[CrossRef\]](#)
54. Yamada, Y.; Nakamura, T.; Endo, M.; Wakamiya, A.; Kanemitsu, Y. Photocarrier recombination dynamics in perovskite $\text{CH}_3\text{NH}_3\text{PbI}_3$ for solar cell applications. *J. Am. Chem. Soc.* **2014**, *136*, 11610–11613. [\[CrossRef\]](#) [\[PubMed\]](#)
55. Zhou, H.; Nie, Z.; Yin, J.; Sun, Y.; Zhuo, H.; Wang, D.; Li, D.; Dou, J.; Zhang, X.; Ma, T. Antisolvent diffusion-induced growth, equilibrium behaviours in aqueous solution and optical properties of $\text{CH}_3\text{NH}_3\text{PbI}_3$ single crystals for photovoltaic applications. *RSC Adv.* **2015**, *5*, 85344–85349. [\[CrossRef\]](#)
56. Maculan, G.; Sheikh, A.D.; Abdelhady, A.L.; Saidaminov, M.I.; Haque, M.A.; Murali, B.; Alarousu, E.; Mohammed, O.F.; Wu, T.; Bakr, O.M. $\text{CH}_3\text{NH}_3\text{PbCl}_3$ Single Crystals: Inverse temperature crystallization and visible-blind UV-Photodetector. *J. Phys. Chem. Lett.* **2015**, *6*, 3781–3786. [\[CrossRef\]](#)
57. Liu, Y.; Ren, X.; Zhang, J.; Yang, Z.; Yang, D.; Yu, F.; Sun, J.; Zhao, C.; Yao, Z.; Wang, B.; et al. 120 mm single-crystalline perovskite and wafers: Towards viable applications. *Sci. China-Chem.* **2017**, *60*, 1367–1376. [\[CrossRef\]](#)
58. Zhumekenov, A.A.; Saidaminov, M.I.; Haque, M.A.; Alarousu, E.; Sarmah, S.P.; Murali, B.; Dursun, I.; Miao, X.H.; Abdelhady, A.L.; Wu, T.; et al. Formamidinium lead halide perovskite crystals with unprecedented long carrier dynamics and diffusion length. *ACS Energy Lett.* **2016**, *1*, 32–37. [\[CrossRef\]](#)
59. Docampo, P.; Ball, J.M.; Darwich, M.; Eperon, G.E.; Snaith, H.J. Efficient organometal trihalide perovskite planar-heterojunction solar cells on flexible polymer substrates. *Nat. Commun.* **2013**, *4*, 1–6. [\[CrossRef\]](#)
60. Rao, H.-S.; Li, W.-G.; Chen, B.-X.; Kuang, D.-B.; Su, C.-Y. In situ growth of 120 cm^2 $\text{CH}_3\text{NH}_3\text{PbBr}_3$ perovskite crystal film on FTO glass for narrowband-photodetectors. *Adv. Mater.* **2017**, *29*, 1602639. [\[CrossRef\]](#)
61. Liu, Y.; Sun, J.; Yang, Z.; Yang, D.; Ren, X.; Xu, H.; Yang, Z.; Liu, S.F. 20-mm-Large Single-Crystalline Formamidinium-Perovskite Wafer for Mass Production of Integrated Photodetectors. *Adv. Optical Mater.* **2016**, *4*, 1829–1837. [\[CrossRef\]](#)
62. Zhao, J.; Kong, G.; Chen, S.; Li, Q.; Huang, B.; Liu, Z.; San, X.; Wang, Y.; Wang, C.; Zhen, Y.; et al. Single crystalline $\text{CH}_3\text{NH}_3\text{PbI}_3$ self-grown on FTO/ TiO_2 substrate for high efficiency perovskite solar cells. *Sci. Bull.* **2017**, *62*, 1173–1176. [\[CrossRef\]](#)
63. Chen, Z.; Turedi, B.; Alsalloum, A.Y.; Yang, C.; Zheng, X.; Gereige, I.; AlSaggaf, A.; Mohammed, O.F.; Bakr, O.M. Single-Crystal MAPbI_3 perovskite solar cells exceeding 21% power conversion efficiency. *ACS Energy Lett.* **2019**, *4*, 1258–1259. [\[CrossRef\]](#)
64. Lian, Z.; Yan, Q.; Lv, Q.; Wang, Y.; Liu, L.; Zhang, L.; Pan, S.; Li, Q.; Wang, L.; Sun, J.L. High-Performance planar-type photodetector on (100) facet of MAPbI_3 single crystal. *Sci. Rep.* **2015**, *5*, 16563. [\[CrossRef\]](#) [\[PubMed\]](#)
65. Xiao, M.; Huang, F.; Huang, W.; Dkhissi, Y.; Zhu, Y.; Etheridge, J.; Gray-Weale, A.; Bach, U.; Cheng, Y.B.; Spiccia, L. A fast deposition-crystallization procedure for highly efficient lead iodide perovskite thin-film solar cells. *Angew. Chem. Int. Ed.* **2014**, *53*, 9898–9903. [\[CrossRef\]](#) [\[PubMed\]](#)
66. Jeon, N.J.; Noh, J.H.; Kim, Y.C.; Yang, W.S.; Ryu, S.; Seok, S.I. Solvent engineering for high-performance inorganic–organic hybrid perovskite solar cells. *Nat. Mater.* **2014**, *13*, 897–903. [\[CrossRef\]](#)
67. Zhang, L.; Liu, Y.; Ye, X.; Han, Q.; Ge, C.; Cui, S.; Guo, Q.; Zheng, X.; Zhai, Z.; Tao, X. Exploring anisotropy on oriented wafers of MAPbBr_3 crystals grown by controlled antisolvent diffusion. *Cryst. Growth Des.* **2018**, *18*, 6652–6660. [\[CrossRef\]](#)
68. Dong, Q.; Song, J.; Fang, Y.; Shao, Y.; Ducharme, S.; Huang, J. Lateral-Structure single-crystal hybrid perovskite solar cells via piezoelectric poling. *Adv. Mater.* **2016**, *28*, 2816–2821. [\[CrossRef\]](#)
69. Dang, Y.; Liu, Y.; Sun, Y.; Yuan, D.; Liu, X.; Lu, W.; Liu, G.; Xia, H.; Tao, X. Bulk crystal growth of hybrid perovskite material $\text{CH}_3\text{NH}_3\text{PbI}_3$. *CrystEngComm* **2015**, *17*, 665–670. [\[CrossRef\]](#)

70. Lv, Q.; Lian, Z.; Li, Q.; Sun, J.-L.; Yan, Q. Formic acid: An accelerator and quality promoter for nonseeded growth of $\text{CH}_3\text{NH}_3\text{PbI}_3$ single crystals. *Chem. Commun.* **2018**, *54*, 1049–1052. [\[CrossRef\]](#)
71. Saidaminov, M.I.; Abdelhady, A.L.; Maculan, G.; Bakr, O.M. Retrograde solubility of formamidinium and methylammonium lead halide perovskites enabling rapid single crystal growth. *Chem. Commun.* **2015**, *51*, 17658–17661. [\[CrossRef\]](#)
72. Zhang, T.; Yang, M.; Benson, E.E.; Li, Z.; van de Lagemaat, J.; Luther, J.M.; Yan, Y.; Zhu, K.; Zhao, Y. A facile solvothermal growth of single crystal mixed halide perovskite $\text{CH}_3\text{NH}_3\text{Pb}(\text{Br}_{1-x}\text{Cl}_x)_3$. *Chem. Commun.* **2015**, *51*, 7820–7823. [\[CrossRef\]](#) [\[PubMed\]](#)
73. Schlipf, J.; Askar, A.M.; Pantle, F.; Wiltshire, B.D.; Sura, A.; Schneider, P.; Huber, L.; Shankar, K.; Müller-Buschbaum, P. Top-Down approaches towards single crystal perovskite solar cells. *Sci. Rep.* **2018**, *8*, 1–8. [\[CrossRef\]](#) [\[PubMed\]](#)
74. Lv, Q.; Lian, Z.; He, W.; Sun, J.-L.; Li, Q.; Yan, Q. A universal top-down approach toward thickness-controllable perovskite single-crystalline thin films. *J. Mater. Chem. C* **2018**, *6*, 4464–4470. [\[CrossRef\]](#)
75. Peng, W.; Wang, L.; Murali, B.; Ho, K.T.; Bera, A.; Cho, N.; Kang, C.F.; Burlakov, V.M.; Pan, J.; Sinatra, L.; et al. Solution-Grown monocrystalline hybrid perovskite films for hole-transporter-free solar cells. *Adv. Mater.* **2016**, *28*, 3383–3390. [\[CrossRef\]](#) [\[PubMed\]](#)
76. Liu, Y.; Zhang, Y.; Yang, Z.; Yang, D.; Ren, X.; Pang, L.; Liu, S. Thinness- and shape-controlled growth for ultrathin single-crystalline perovskite wafers for mass production of superior photoelectronic devices. *Adv. Mater.* **2016**, *28*, 9204–9209. [\[CrossRef\]](#) [\[PubMed\]](#)
77. Agiorgousis, M.L.; Sun, Y.-Y.; Zeng, H.; Zhang, S. Strong covalency-induced recombination centers in perovskite solar cell material $\text{CH}_3\text{NH}_3\text{PbI}_3$. *J. Am. Chem. Soc.* **2014**, *136*, 14570–14575. [\[CrossRef\]](#) [\[PubMed\]](#)
78. Cheng, X.; Yang, S.; Cao, B.Q.; Tao, X.T.; Chen, Z.L. Single crystal perovskite solar cells: Development and perspectives. *Adv. Funct. Mater.* **2020**, *30*, 1905021. [\[CrossRef\]](#)
79. Liu, Y.; Dong, Q.; Fang, Y.; Lin, Y.; Deng, Y.; Huang, J. Fast growth of thin MAPbI_3 crystal wafers on aqueous solution surface for efficient lateral-structure perovskite solar cells. *Adv. Funct. Mater.* **2019**, *29*, 1807707. [\[CrossRef\]](#)
80. Ponseca, C.S., Jr.; Savenije, T.J.; Abdellah, M.; Zheng, K.; Yartsev, A.; Pascher, T.; Harlang, T.; Chabera, P.; Pullerits, T.; Stepanov, A.; et al. Organometal halide perovskite solar cell materials rationalized: Ultrafast charge generation, high and microsecond-long balanced mobilities, and slow recombination. *J. Am. Chem. Soc.* **2014**, *136*, 5189–5192. [\[CrossRef\]](#)
81. Ye, F.; Lin, H.; Wu, H.; Zhu, L.; Huang, Z.; Ouyang, D.; Niu, G.; Choy, W.C. High-Quality cuboid $\text{CH}_3\text{NH}_3\text{PbI}_3$ single crystals for high performance X-ray and photon detectors. *Adv. Funct. Mater.* **2019**, *29*, 1806984. [\[CrossRef\]](#)
82. Zou, Y.; Zou, T.; Zhao, C.; Wang, B.; Xing, J.; Yu, Z.; Cheng, J.; Xin, W.; Yang, J.; Yu, W.; et al. A highly sensitive single crystal perovskite–graphene hybrid vertical photodetector. *Small* **2020**, *16*, 2000733. [\[CrossRef\]](#) [\[PubMed\]](#)
83. Lin, Q.; Armin, A.; Burn, P.L.; Meredith, P. Near infrared photodetectors based on sub-gap absorption in organohalide perovskite single crystals. *Laser Photonics Rev.* **2016**, *10*, 1047–1053. [\[CrossRef\]](#)
84. Zhang, Y.; Liu, Y.; Xu, Z.; Ye, H.; Li, Q.; Hu, M.; Yang, Z.; Liu, S.F. Two-Dimensional $(\text{PEA})_2\text{PbBr}_4$ perovskite single crystals for a high performance UV-detector. *J. Mater. Chem. C* **2019**, *7*, 1584–1591. [\[CrossRef\]](#)
85. Xiao, X.; Dai, J.; Fang, Y.; Zhao, J.; Zheng, X.; Tang, S.; Rudd, P.N.; Zeng, X.C.; Huang, J. Suppressed ion migration along the in-plane direction in layered perovskites. *ACS Energy Lett.* **2018**, *3*, 684–688. [\[CrossRef\]](#)
86. Gan, Z.; Wen, X.; Chen, W.; Zhou, C.; Yang, S.; Cao, G.; Ghiggino, K.P.; Zhang, H.; Jia, B. The dominant energy transport pathway in halide perovskites: Photon recycling or carrier diffusion? *Adv. Energy Mater.* **2019**, *9*, 1900185. [\[CrossRef\]](#)
87. Wei, H.; Huang, J. Halide lead perovskites for ionizing radiation detection. *Nat. Commun.* **2019**, *10*, 1066. [\[CrossRef\]](#)
88. Zhuang, R.; Wang, X.; Ma, W.; Wu, Y.; Chen, X.; Tang, L.; Zhu, H.; Liu, J.; Wu, L.; Zhou, W.; et al. Highly sensitive X-ray detector made of layered perovskite-like $(\text{NH}_4)_3\text{Bi}_2\text{I}_9$ single crystal with anisotropic response. *Nat. Photonics* **2019**, *13*, 602–608. [\[CrossRef\]](#)
89. Wei, H.; DeSantis, D.; Wei, W.; Deng, Y.; Guo, D.; Savenije, T.J.; Cao, L.; Huang, J. Dopant compensation in alloyed $\text{CH}_3\text{NH}_3\text{PbBr}_{3-x}\text{Cl}_x$ perovskite single crystals for gamma-ray spectroscopy. *Nat. Mater.* **2017**, *16*, 826–833. [\[CrossRef\]](#)

90. Lehner, A.J.; Fabini, D.H.; Evans, H.A.; Hébert, C.A.; Smock, S.R.; Hu, J.; Wang, H.; Zwanziger, J.W.; Chabiny, M.L.; Seshadri, R. Crystal and electronic structures of complex bismuth iodides $A_3Bi_2I_9$ ($A = K, Rb, Cs$) related to perovskite: Aiding the rational design of photovoltaics. *Chem. Mater.* **2015**, *27*, 7137–7148. [\[CrossRef\]](#)
91. Liu, Y.; Zhang, Y.; Zhao, K.; Yang, Z.; Feng, J.; Zhang, X.; Wang, K.; Meng, L.; Ye, H.; Liu, M.; et al. A 1300 mm² ultrahigh-performance digital imaging assembly using high-quality perovskite single crystals. *Adv. Mater.* **2018**, *30*, 1707314. [\[CrossRef\]](#)
92. Yao, F.; Peng, J.; Li, R.; Li, W.; Gui, P.; Li, B.; Liu, C.; Tao, C.; Lin, Q.; Fang, G. Room-Temperature liquid diffused separation induced crystallization for high-quality perovskite single crystals. *Nat. Commun.* **2020**, *11*, 1–9. [\[CrossRef\]](#) [\[PubMed\]](#)
93. Zhang, Y.; Liu, Y.; Xu, Z.; Ye, H.; Yang, Z.; You, J.; Liu, M.; He, Y.; Kanatzidis, M.G.; Liu, S.F. Nucleation-controlled growth of superior lead-free perovskite $Cs_3Bi_2I_9$ single-crystals for high-performance X-ray detection. *Nat. Commun.* **2020**, *11*, 1–11.
94. Zhou, L.; Liao, J.F.; Huang, Z.G.; Wei, J.H.; Wang, X.D.; Li, W.G.; Chen, H.Y.; Kuang, D.B.; Su, C.Y. A highly red-emissive lead-free indium-based perovskite single crystal for sensitive water detection. *Angew. Chem. Int. Ed.* **2019**, *58*, 5277–5281. [\[CrossRef\]](#)
95. Chen, P.; Bai, Y.; Wang, S.; Lyu, M.; Yun, J.H.; Wang, L. In situ growth of 2D perovskite capping layer for stable and efficient perovskite solar cells. *Adv. Funct. Mater.* **2018**, *28*, 1706923. [\[CrossRef\]](#)
96. Murali, B.; Dey, S.; Abdelhady, A.L.; Peng, W.; Alarousu, E.; Kirmani, A.R.; Cho, N.; Sarmah, S.P.; Parida, M.R.; Saidaminov, M.I.; et al. Surface restructuring of hybrid perovskite crystals. *ACS Energy Lett.* **2016**, *1*, 1119–1126. [\[CrossRef\]](#)
97. Wei, W.; Zhang, Y.; Xu, Q.; Wei, H.; Fang, Y.; Wang, Q.; Deng, Y.; Li, T.; Gruverman, A.; Cao, L.; et al. Monolithic integration of hybrid perovskite single crystals with heterogenous substrate for highly sensitive X-ray imaging. *Nat. Photonics* **2017**, *11*, 315–321. [\[CrossRef\]](#)
98. Geng, X.; Wang, F.; Tian, H.; Feng, Q.; Zhang, H.; Liang, R.; Shen, Y.; Ju, Z.; Gou, G.Y.; Deng, N.; et al. Ultrafast photodetector by integrating perovskite directly on silicon wafer. *ACS Nano* **2020**, *14*, 2860–2868. [\[CrossRef\]](#)



© 2020 by the authors. Licensee MDPI, Basel, Switzerland. This article is an open access article distributed under the terms and conditions of the Creative Commons Attribution (CC BY) license (<http://creativecommons.org/licenses/by/4.0/>).